BAMS Article

"Godzilla," the Extreme African Dust Event of June 2020: Origins, Transport, and Impact on Air Quality in the Greater Caribbean Basin

O. L. Mayol-Bracero,[a] J. M. Prospero,[b] B. Sarangi,[c] E. Andrews,[d,e] P. R. Colarco,[f] E. Cuevas,[g] L. Di Girolamo,[h] R. D. Garcia,[g,i] C. Gaston,[b] B. Holben,[f] L. A. Ladino,[j] P. León,[c] R. Losno,[k] O. Martínez,[l] B. L. Martínez-Huertas,[c] P. Méndez-Lázaro,[m] J. Molinie,[n] F. Muller-Karger,[o] D. Otis,[o] G. Raga,[j] A. Reyes,[p] J. Rosas Nava,[c] D. Rosas,[q] A. Sealy,[p] I. Serikov,[r] D. Tong,[s] E. Torres-Delgado,[c] H. Yu,[f] and P. Zuidema[b]

KEYWORDS:
Dust or dust storms;
Climate;
Satellite observations;
Surface observations;
Aerosols/particulates;
Air quality and health

ABSTRACT: In June 2020, the tropical Atlantic and the Caribbean Basin were affected by a series of African dust outbreaks unprecedented in size and intensity. These events, informally named "Godzilla," coincided with CALIMA, a large field campaign, offering a rare opportunity to assess the impact of African dust on air quality in the Greater Caribbean Basin. Network measurements of respirable particles (i.e., PM_{10} and $PM_{2.5}$) showed that dust significantly degraded regional air quality and increased the risk to public health in the Caribbean, the southern United States, northern South America, and Central America. CALIMA examined the meteorological context of Godzilla dust events over North Africa and how these conditions might relate to the greatly increased dust emissions and enhanced transport to the Americas. Godzilla was linked to strong pressure anomalies over West Africa, resulting in a large-scale geostrophic wind anomaly at 700 hPa over North Africa. We used surface-based and columnar measurements to test the performance of two frequently used aerosol forecast models: the NASA Goddard Earth Observing System (GEOS) and Weather Research and Forecasting Model coupled with Chemistry (WRF-Chem) models. The models showed some skills but differed substantially between their forecasts, suggesting large uncertainties in these forecasts that are critical for issuing early warnings of health-threatening dust events. Our results demonstrate the value of an integrated approach in characterizing the spatial and temporal variability of African dust transport and assessing its impact on regional air quality. Future studies are needed to improve models and to track the long-term changes in dust transport from Africa under a changing climate.

DOI: 10.1175/BAMS-D-24-0045.1
Corresponding author: Olga L. Mayol-Bracero, omayol@bnl.gov
Supplemental information related to this paper is available at the Journals Online website: https://doi.org/10.1175/BAMS-D-24-0045.s1.

Manuscript received 8 February 2024, in final form 20 February 2025, accepted 14 April 2025

SIGNIFICANCE STATEMENT: Every year, vast quantities of African dust are transported across the Atlantic to the Caribbean Basin. During these events, respirable dust concentrations often exceed the air quality standards established by the United States EPA and the World Health Organization. We discuss the record-breaking June 2020 "Godzilla" dust events in terms of measurements made during a large-scale surface-based field campaign (CALIMA). During CALIMA, we made aerosol measurements at sites throughout the Caribbean Basin. We used satellite and aerosol model products to interpret the data and understand the meteorological processes that affect dust emissions in Africa and the subsequent transport to the Americas. Models could provide advanced warnings of health-threatening dust events, thereby enabling public health officials to issue health risk alerts.

AFFILIATIONS: [a] Brookhaven National Laboratory, Upton, New York; [b] Rosenstiel School of Marine, Atmospheric and Earth Science, University of Miami, Miami, Florida; [c] Department of Environmental Science, University of Puerto Rico-Rio Piedras Campus, San Juan, Puerto Rico; [d] NOAA/Global Monitoring Laboratory, Boulder, Colorado; [e] Cooperative Institute for Research in Environmental Sciences, University of Colorado Boulder, Boulder, Colorado; [f] NASA Goddard Space Flight Center, Greenbelt, Maryland; [g] Izaña Atmospheric Research Center, State Meteorological Agency of Spain (AEMET), Santa Cruz de Tenerife, Spain; [h] University of Illinois Urbana–Champaign, Urbana, Illinois; [i] TRAGSATEC, Madrid, Spain; [j] Instituto de Ciencias de la Atmósfera y Cambio Climático, Universidad Nacional Autónoma de México, Mexico City, México; [k] University of Paris, IPGP, Paris, France; [l] NOAA/NWS, San Juan Office, Carolina, Puerto Rico; [m] Environmental Health Department, University of Puerto Rico-Medical Sciences Campus, San Juan, Puerto Rico; [n] Laboratoire de Recherche en Geosciences et Energies, Université des Antilles, Guadeloupe, France; [o] Institute for Marine Remote Sensing, University of South Florida, Tampa, Florida; [p] Caribbean Institute for Meteorology and Hydrology, St. James, Barbados; [q] Facultad de Química, Universidad Autónoma de Yucatán, Mérida, México; [r] Max Planck Institute for Meteorology, Hamburg, Germany; [s] George Mason University, Fairfax, Virginia

1. Introduction

a. Background. The world's largest and most persistently active dust sources are in North Africa, accounting for 28%–69% of global emissions (Zhao et al. 2022). Dust from the Sahara and Sahel is transported over vast areas of the North Atlantic and the Greater Caribbean Basin (GCB; Robertson and Cramer 2014), including the southeastern United States (Prospero et al. 1987; Gaztambide-Géigel 2004; Prospero and Mayol-Bracero 2013) and northern South America (Prospero et al. 1981; Prospero 1999; Prospero and Mayol-Bracero 2013; Yu et al. 2015a). These particles can affect weather, human health, air quality, and marine and terrestrial ecosystems, and they play an important role in climate (e.g., Kok et al. 2023; Dunion and Velden 2004; Twohy et al. 2009; Evan et al. 2011; Okin et al. 2011; Prospero and Mayol-Bracero 2013; Prospero et al. 2014; West et al. 2016; Zhang et al. 2016; Tong et al. 2023).

Exposure to dust has been associated with many health impacts, such as increased risks of asthma, fungal infections, and premature death (Lwin et al. 2023; Tong et al. 2023). However, the health impact of African dust in the GCB has not been well studied. Some studies suggest that dust impacts asthma rates which are very high in some locations in the GCB (Monteil et al. 2005; Cadelis et al. 2014; Akpinar-Elci et al. 2015). However, such associations were not found in Barbados (Prospero et al. 2008). Puerto Ricans experience

the highest prevalence of asthma in the United States (Alicea-Alvarez et al. 2014), but the connection to African dust is unclear.

African dust events and their impact on air quality over GCB have been well documented in satellite studies (e.g., Yu et al. 2015a,b, 2019) and ground measurements (Prospero et al. 2014). The satellite-borne Cloud–Aerosol Lidar with Orthogonal Polarization (CALIOP) shows that about 40 million tons of African dust are annually transported to the GCB mostly in the boreal summer. Dust events typically extend from the surface to an altitude of several kilometers as validated by surface-based lidars (e.g., Gutleben and Gross 2021). Within these air masses, much of the dust is carried in an elevated hot–dry layer that has its origins over the Sahara Desert and, which, consequently, is named the Saharan air layer (SAL; Carlson and Prospero 1972; Prospero et al. 2021). From about 25% (Prospero and Carlson 1972) to 40% (Yu et al. 2015a) of the total column dust mass is transported within the lowest 1 km of the atmosphere and is therefore relevant to air quality issues (Yu et al. 2015a). The impact of African dust on air quality is usually assessed based on measurements of surface PM_{10} and $PM_{2.5}$ (particulate matter with aerodynamic diameters < 10 and <2.5 μm, respectively). $PM_{2.5}$ and PM_{10} are routinely measured as a part of national air quality monitoring including sites in the GCB. At Guadeloupe, Martinique, and Cayenne (French Guiana), PM_{10} exceeded the World Health Organization (WHO) 24-h guidelines of 45 $\mu g\ m^{-3}$ on 10% of days annually and as high as 20%–35% of days during the dust season, typically May–September (Prospero et al. 2014). These exceedance rates are comparable to those due to pollution in large urban areas in Europe and the United States (Prospero et al. 2014). Sites in Puerto Rico, Florida, Texas, and Barbados show similar $PM_{2.5}$ exceedance rates (Prospero et al. 2001; Bozlaker et al. 2013; Prospero et al. 2014; Yu et al. 2021) (see S1 in the online supplemental material for air quality guidelines).

Numerical models are useful tools for predicting temporal and spatial variations of aerosol events and assisting air quality and health agencies in issuing early warnings. Numerous research and operational modeling systems have provided dust forecasts for early warning over the Americas including the GCB region (Xian et al. 2019; Tong et al. 2023). It is difficult to assess the accuracy of dust forecasting models because of the lack of airborne or in situ aerosol data. This, in turn, limits our ability to plan for the arrival of dust events. Many studies have highlighted the need for observations to constrain and improve models (e.g., Evan et al. 2014; Kim et al. 2014; Yu et al. 2021; Kok et al. 2023; Tong et al. 2023). The study of intercontinental transport events, as in the case of African dust, is more challenging than the study of the local or regional dust because of the temporal and spatial scale of these events and the fragmented observations in the receptor region. The measurements in CALIMA address many of these issues.

b. CALIMA. The primary objective of CALIMA (calima: Spanish for "haze") was to advance our understanding of the impact of African dust on air quality in the GCB. More specifically, CALIMA aims 1) to characterize and quantify the large-scale distribution of African dust in the GCB through measurements of dust concentrations made at sites throughout the region; 2) to use satellite products to visualize the large-scale movement of dust outbreaks from the source areas to the receptor sites; 3) to relate the occurrence and fate of dust outbreaks in terms of synoptic meteorological conditions; and 4) to use these various observations to evaluate dust forecast models, with the ultimate goal of having dust forecast models that are better in predicting the impact of dust events in the air quality of the region. CALIMA began a scheduled intensive field campaign in summer 2020'. Fortuitously, the campaign was in progress when the Godzilla dust event occurred in June 2020. Because of the great density, extent, duration, and, especially, shape of the dust plume (Fig. 1), one of our coauthors (JMP) named it "Godzilla," after the fictional monster. To our knowledge, this is the first and only "named" dust storm (see S2 for the Godzilla name history).

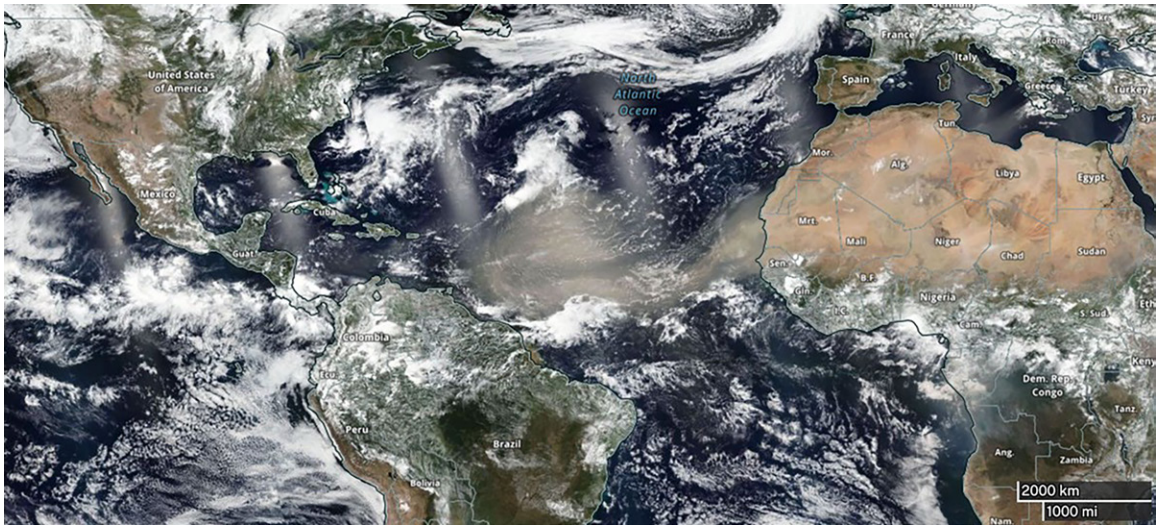

Fig. 1. Dust plumes over the tropical Atlantic and the GCB on 20 Jun 2020 observed by the VIIRS sensor aboard the *Suomi NPP* satellite, visualized with NASA WorldView. VIIRS is a polar-orbiting satellite. The coherent bright bars, located at a slight angle from the vertical, are due to the specular reflection of sunlight from the ocean surface; a bar is generated on each overpass.

CALIMA undertook an integrated regional approach that involved aerosol ground-based measurements in multiple locations across the GCB coupled with satellite observations and forecast models. Here, 1) we use satellite observations and dust forecast models to understand the meteorological context that led to the Godzilla dust event; 2) we compare dust model forecasts with ground-based measurements to assess the impacts of Godzilla on air quality in the GCB; and 3) we put Godzilla in historical context using long-term in situ measurements at Barbados and Puerto Rico and satellite observations, i.e., the 22-yr record of Multiangle Imaging SpectroRadiometer (MISR) and Moderate Resolution Imaging Spectroradiometer (MODIS) satellite observations.

2. Methodology

a. Sampling locations and strategy. The CALIMA study area extends over the GCB (Fig. 2). The region encompasses a total of 28 countries and ~40 million people (Nkemdirim 1997; Crews and Esposito 2020). We focus on the measurements performed in summer 2020. The main ground-based CALIMA measurements were at Cayenne (CAY), Barbados (BAR), Martinique (MAR), Guadeloupe (GUA), Cape San Juan–Puerto Rico (CSJ–PR), Merida–Mexico (MEDA–MEX), and Miami (MIA–USA) (Fig. 2). We used air quality measurement data from seven additional locations: Trinidad and Tobago (T & T or TRI and TOB, one station on each island), three more stations in the southern United States {Jacksonville [northeastern Florida (FLO-NE)], Tallahassee [northwestern Florida (FLO-NW)], and Houston (HOU–USA)], and three stations from Puerto Rico [Cataño (CAT–PR), Mayagüez (MAYA–PR), and Guaynabo (GUAY–PR)].

The ground-based aerosol measurements (e.g., PM_{10} and $PM_{2.5}$ mass concentrations, light scattering and absorption coefficients, visibility, dust concentrations), column measurements of aerosol optical depth (AOD), satellite observations, and dust forecast models are listed in Table 1 and described below.

1) Ground aerosol in situ measurements. The PM_{10} and $PM_{2.5}$ mass concentrations were measured from 12 ground stations (Fig. 2): Atmo Guyane, Cayenne; Point Lisas, Trinidad; Signal Hill, Tobago; Station Robert-Bourg, Martinique; Université des Antilles, Guadeloupe; Cape San Juan–Puerto Rico; Puerto Rico U.S.-EPA sites (Cataño, Mayagüez, and Guaynabo),

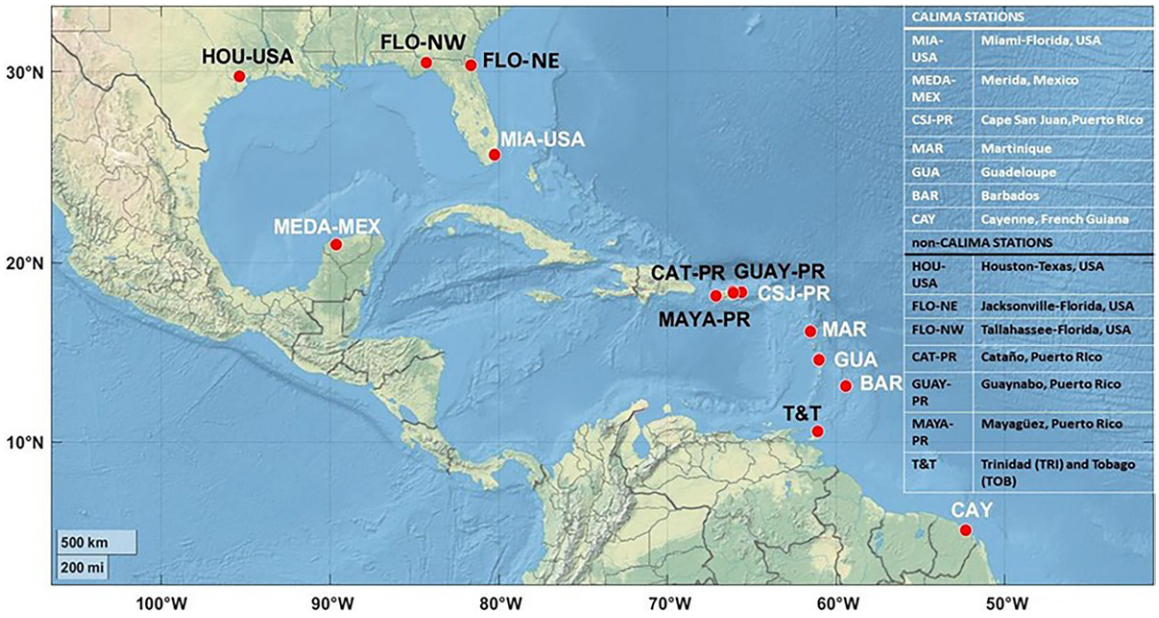

Fig. 2. Map of the GCB, defined as encompassing the island nations and Caribbean coastal states, including the southeastern United States and central and northern South America, showing the CALIMA 2020 sampling locations: CAY, T & T, Ragged Point–BAY, MAR, GUA, CSJ–PJ, CAT–PR, MAYA–PR, GUAY-PR, MEDA–MEX, MIA, Jacksonville, Tallahassee, and HOU. The names in black are contributing stations but non-CALIMA stations. The map is created using Natural Earth in MATLAB.

National Autonomous University of Mexico, and Merida, Mexico; Oyster Creek, Texas; and Jacksonville, Florida. At CSJ–PR, an optical particle counter (OPC; MetOne 237B particle counter) was used to determine the PM_{10} mass concentrations. PM_{10} was computed from the OPC assuming spherical particles, a particle density (2.2 g cm^{-3}) and assuming the cut-off diameter of the sampling "head" was 10 μm. The PM_{10} is obtained as the integrated mass of all bins below 10 μm. The other stations in Puerto Rico (CAT–PR, GUAY–PR, and MAYA–PR) and Houston used PM_{10} high-volume samplers (TISCH serial no. 3426). GUA, MAR, CAY, and FLO-NE used the tapered element oscillating microbalance (TEOM; Thermo Scientific, Model 1400ab). Trinidad and Tobago used the Teledyne API Model T640. The MEDA–MEX site used the beta attenuation mass monitor (BAM) 1020 with a PM_{10} inlet with very-sharp-cut cyclone (VSCC; ThermoScientific, Model: FH62C14). Dust mass concentrations at CSJ–PR, BAR,

Table 1. CALIMA (a) ground-based measurements, (b) satellite observations, and (c) dust forecast models.

(a) Ground-based observations	(b) Satellite observations	(c) Forecast models
Aerosol mass concentrations (PM_{10}, $PM_{2.5}$)	VIIRS, MODIS, and MISR: AOD, 550 nm, total and segregated by aerosol size and shape	GEOS: global model. DSC and column-integrated AOD, vertical profiles of dust extinction and mass mixing ratio
AOD at 500 nm	CALIPSO: Column optical depth 532 nm and extinction coefficient 532 nm	WRF-Chem: regional model. DSC and column-integrated AOD, surface $PM_{2.5}$ and PM_{10} concentration
Aerosol optical properties (scattering, absorption, visibility)	SEVIRI: RGB (R–G–B) composite based upon infrared channels (IR8.7, IR10.8, and IR12.0) data	
Aerosol vertical structure–lidars		
Meteorological parameters: temperature, relative humidity, wind speed, wind direction, and BLH		
Dust concentrations (TSP)		

and MIA–USA were obtained based on the gravimetric analysis of total suspended particle (TSP)/PM_{10} filters as described in Zuidema et al. (2019) and Prospero (1999). Dust in this case is defined as the ash residue weight, less the filter blank.

2) Ground-based aerosol remote sensing. The column aerosol optical depths at 500 nm were accessed from seven Aerosol Robotic Network (AERONET; Sun Photometer CE318, CIMEL, level 2) sites (e.g., CSJ–PR, GUA, BAR, MEDA–MEX, MIA–USA, HOU–USA, FLO-NW) in the GCB and southern United States (Holben et al. 1998). The wavelength-dependent aerosol optical properties (e.g., scattering coefficients, absorption coefficients, and scattering Ångström exponent) were obtained from the CSJ–PR site in Puerto Rico (Andrews et al. 2019). The aerosol scattering coefficient at three wavelengths (450, 500, and 700 nm) was measured by a nephelometer (TSI 3563), and the absorption coefficient was measured by a continuous light absorption photometer (CLAP) at three wavelengths (467, 528, and 652 nm). The aerosol scattering Ångström exponent (SAE; wavelength pair 450–700 nm) was calculated from the aerosol scattering coefficients obtained from the nephelometer.

The aerosol vertical structure was assessed from a ground-based micropulse lidar with depolarization operating at Miami and a Raman lidar with depolarization in Barbados (Stevens et al. 2016; Delgadillo et al. 2018).

3) Weather observations. In Puerto Rico, the surface meteorological parameters (e.g., temperature, relative humidity, wind speed, wind direction) were drawn from a weather station (Vaisala WXT530) at CSJ–PR. The visibility data were obtained from a sensor (Vaisala PWD 20) located at the same elevation as the weather station. The boundary layer height (BLH) was estimated based on the observations from the land-based radiosondes launched at the National Weather Service Forecast Office in San Juan, Puerto Rico (WFO SJU, 18.43°N, 65.61°W). The Barbados and Miami sonde data are available online (https://weather.uwyo.edu/upperair/sounding.html).

4) Satellite observations. Satellite observations included the measurements of aerosol optical depth at 500 nm using the Visible Infrared Imaging Radiometer Suite (VIIRS; level 1.5) and Level 1 and Atmosphere Archive and Distribution System (LAADS) with deep blue (DB) aerosol and dark target (DT) aerosol sets (Levy et al. 2015) and the MODIS *Terra* and *Aqua* spacecraft with deep blue aerosol and dark target aerosol sets (Levy et al. 2015). The aerosol optical depth with total and segregated by aerosol size and shape was obtained from the MISR on the *Terra* satellite (Kahn et al. 2009; Garay et al. 2020). The column aerosol optical depth and extinction coefficient at 532 nm were obtained from space-based *Cloud–Aerosol Lidar and Infrared Pathfinder Satellite Observations* (CALIPSO) with the CALIOP that performs global profiling of aerosol and clouds in the troposphere and lower stratosphere—level 2, version 3 (Winker et al. 2009). The red–green–blue (RGB) composite based upon infrared channel (IR8.7, IR10.8, and IR12.0) data was accessed from Spinning Enhanced Visible and Infrared Imager (SEVIRI), which is a scanning radiometer (Banks et al. 2019).

5) Dust forecast models. Dust forecasts were provided through collaborations with the NASA Goddard Space Flight Center (GSFC) (https://www.nasa.gov/goddard) and the Caribbean Institute for Meteorology and Hydrology (CIMH) (https://www.cimh.edu.bb/). The NASA Goddard Earth Observing System (GEOS) model was used to forecast dust surface concentration and column-integrated aerosol optical depths, vertical profiles of dust extinction, and mass mixing ratio (Molod et al. 2015). The near-real-time GEOS "forward processing" model is used here, which has a global ~12.5-km horizontal resolution and 72 hybrid sigma vertical levels extending from the surface to ~80 km (1 Pa). GEOS produces several

forecasts each day, the longest being a 10-day forecast initialized at 0000 UTC: Products are typically available at 1-h frequency for the surface or column-integrated fields and 3-h frequency for vertical quantities. Aerosol data assimilation is based on assimilation of total aerosol optical depth derived from near-real-time MODIS aerosol products (Xian et al. 2019). The Weather Research and Forecasting Model coupled with Chemistry (WRF-Chem) was used to forecast dust surface concentration and total aerosol optical depth (Skamarock et al. 2005). The WRF-Chem is a regional model that has two dynamical cores, 40 vertical levels extending from the surface to 5 hPa, a 27-km horizontal spatial resolution, and time resolution each 3 h for 7 days of forecast. Additional information for these two models is provided in S3.

3. Results and discussion

In this section, we present 1) the satellite observations (Table 1) that preceded the Godzilla dust event and those during the event, 2) Godzilla's meteorological context, 3) its altitude, 4) its models' predictions, 5) its impact on air quality, and 6) and its record levels for different aerosol properties.

a. Satellite observations of the Godzilla dust event. Satellite retrievals (see Table 1) showed an unusually high frequency of dust intrusions over the North Atlantic in June 2020. The evolving nature of Godzilla is seen in daily VIIRS *Suomi NPP* satellite images (Figs. S4 and S5). A dense dust plume emerged from the African coast on 7 June (Fig. S4), but it did not travel far. From 9 to 14 June, several more dust plumes emerged from the coast, but none reached the GCB. On 15 June, an immense plume filled much of the eastern Atlantic (Fig. S4). By 18 June, the dust event, comprised of two dust pulses, had advanced to the middle of the tropical Atlantic (Fig. S4). It eventually impacted much of the GCB from 21 June to 1 July. On 23 June, while the first dust plume was entering the eastern Caribbean (Fig. S5), a second plume emerged from Africa, but it was less intense, and the aerial coverage was less than the first (Yu et al. 2021). The second dust plume affected the GCB from 26 June to 1 July. In the following section, we present the meteorological context for the Godzilla dust event.

b. Meteorological context. Enhanced dust transport to the tropical Atlantic can be linked to differences in anomalies of the geopotential heights at 700 hPa between the subtropical (over Morocco) and tropical (over Nigeria) regions of North Africa. These differences are expressed as the North African dipole intensity (NAFDI) index (Rodríguez et al. 2015; Cuevas et al. 2017). A strong NAFDI (higher pressure over the Sahara and lower pressure over the tropics) can lead to increased wind speeds, more vigorous atmospheric circulation, and enhanced dust emissions. Negative phases of NAFDI result in dust export to the western Mediterranean (Cuevas et al. 2017). A positive NAFDI enhances transport to the tropical North Atlantic (Rodríguez et al. 2015; Schepanski et al. 2017). NAFDI changes phase on a 7–10-day cycle, which is broadly consistent with the pulsing frequency of dust plumes emerging from the coast as observed by satellites.

NAFDI is also closely connected to the Saharan heat low (SHL) longitudinal position, which modulates numerous mesoscale meteorological processes that can cause Saharan dust mobilization (Cuevas et al. 2017 and references therein). The east phase of the SHL corresponds to the negative NAFDI phase, and vice versa. We use the NAFDI daily index (NAFDIDI) and the daily SHL longitudinal shift index (SHLLSI; Cuevas et al. 2017) to understand the meteorological conditions behind the Godzilla dust events. In June 2020, negative values of both NAFDIDI and SHLLSI were registered until 13 June (Fig. 3a). On 14 June, NAFDI sharply changed to a positive phase, except the "anomalous" negative values of NAFDIDI and SHLLSI around 18 June.

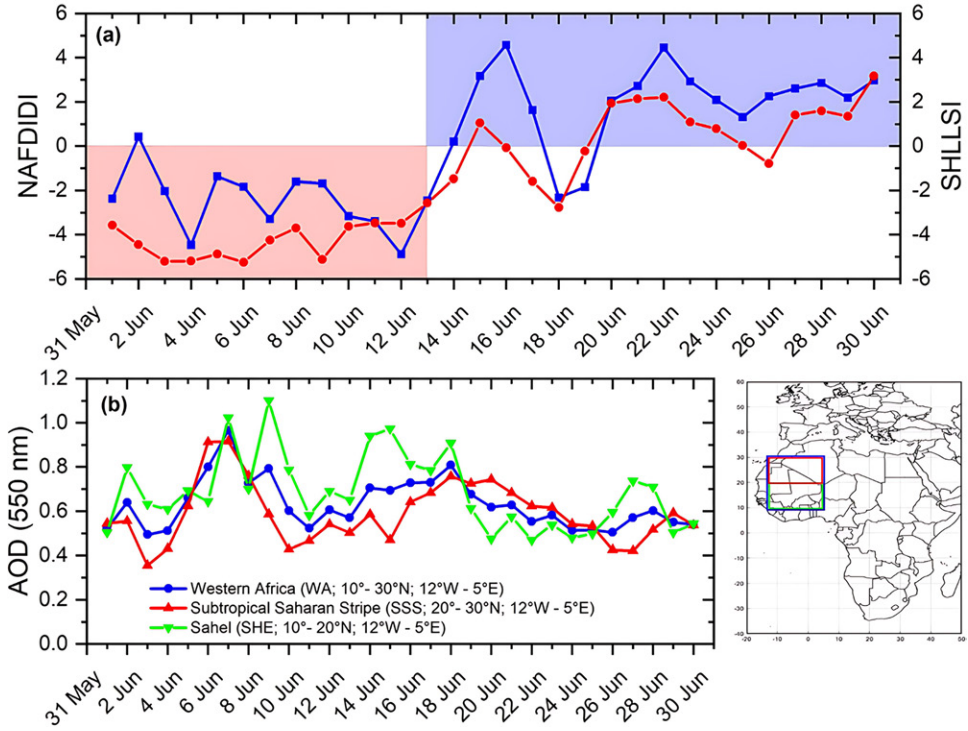

FIG. 3. Time series of (a) NAFDIDI and the SHLLSI, and (b) daily MODIS AOD at 550 nm for June 2020 over the African dust source regions.

Next, we investigate the linkage between meteorological processes and dust mobilization in the main dust source regions using the NAFDI phase and satellite observations. The primary dust sources impacting the GCB are in the Sahel and the western Sahara (Zhao et al. 2022; Prospero and Mayol-Bracero 2013, and references herein), referred to as the SHE region (10°–20°N, 12°W–5°E). Another dust source region is the so-called subtropical Saharan stripe (SSS; 20°–30°N; 12°W–5°E) region, as described by Rodríguez et al. (2015), and where northeast winds with moderate-to-strong average wind speed are observed under positive NAFDI. To identify where dust is mobilized in the Sahara and Sahel regions in June 2020, we examined the daily 15-min EUMETSAT SEVIRI dust–RGB imagery (Met Office: EUMETSAT 2022), following Schepanski et al. (2007, 2009) (Fig. S6), which confirm the origins of dust sources over the SSS and SHE regions. We next elaborate in detail the relationship between dust loading, indicated by MODIS AOD, and the meteorological conditions.

1) NAFDI NEGATIVE PHASE. In the first 3 days of June 2020, a strong cutoff low centered between the Azores and the Iberian Peninsula evolved into a deep trough visible from 850 to 200 hPa (not shown here) with a NE–SW axis that extended from midlatitudes (40°N) to Cape Verde along West Africa (Fig. 4a). This upper-level trough between the North Atlantic subtropical high (NASH) and the North African high is a characteristic pattern of the geopotential height at 700 hPa during the negative phases of NAFDI (Cuevas et al. 2017). Francis et al. (2020) reported this trough at 850 hPa. Such troughs are associated with midlatitude Rossby waves (Chauvin et al. 2010).

Between 4 and 8 June, and coinciding with a deepening and maximum elongation to the south of the trough at 700 hPa, very high clouds associated with mesoscale convective systems (MCSs) and large areas of dust (in pink) are clearly seen to develop in a matter of hours in the SHE and SSS, as shown by SEVIRI RGB–dust imagery. This region shows several AOD peaks (Fig. 3b), consistent with the great quantities of dust being uplifted by short-lived atmospheric processes, like MCSs. This results in a period of days in June 2020 with the highest average AOD values. This was most likely caused by the upper trough present between 4 and 13 June since

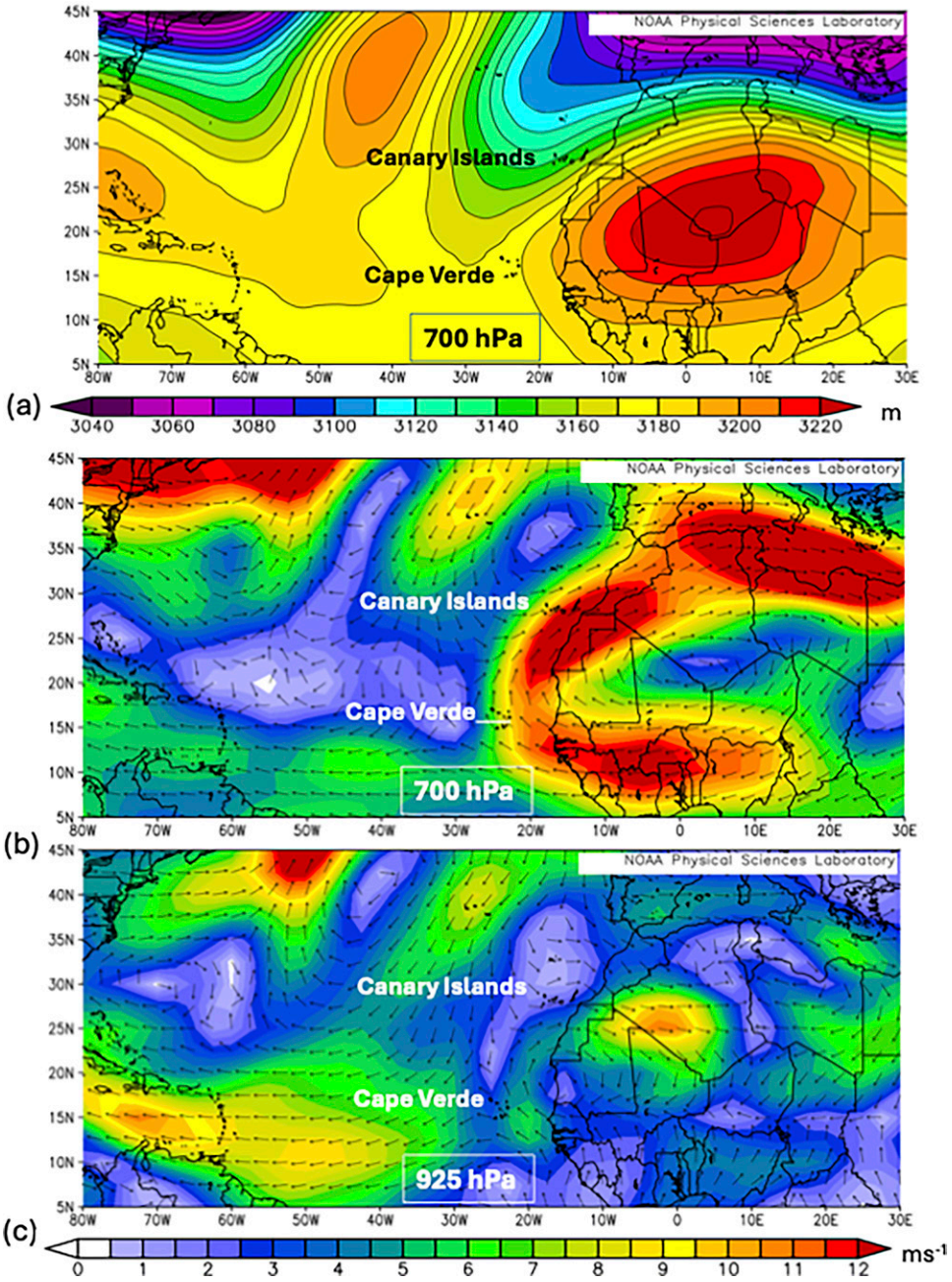

Fig. 4. Time-averaged (a) geopotential height at 700 hPa (m), (b) vector wind at 700 hPa, and (c) vector wind at 925 hPa for the period 1–13 Jun 2020, in the geographical domain 5°–45°N, 80°W–30°E, under the negative NAFDI phase (source: NCEP/NCAR reanalysis).

the strong upper-level midlatitude troughs in the Atlantic–Africa sector caused a significant northward shift of the intertropical discontinuity (ITD) (Ward et al. 2023). From 11 to 13 June, additional dust contributions from MCSs were still observed but with much lower intensity.

During the period 4–13 June 2020, a large amount of dust was present over the SSS and the SHE (Fig. 3b), coinciding with several dense short-range dust plumes emerging from the African coast (Fig. S4); the dust remained confined over the continent and the ocean close to the coastline (<500-km distance) (Fig. 5a) because of wind recirculation over northern Africa, typical of the negative NAFDI phase (Cuevas et al. 2017).

Indeed, under the negative phase NAFDI, wind fields prevent the transport of dust into the Atlantic throughout 1–13 June, as shown in Figs. 4b and 4c. A moderate-to-strong easterly wind corridor is observed over the Sahel at 700 hPa (Fig. 4b). When the plume reaches the Atlantic Ocean, at a maximum distance of about 500 km from the coast, the flow curves

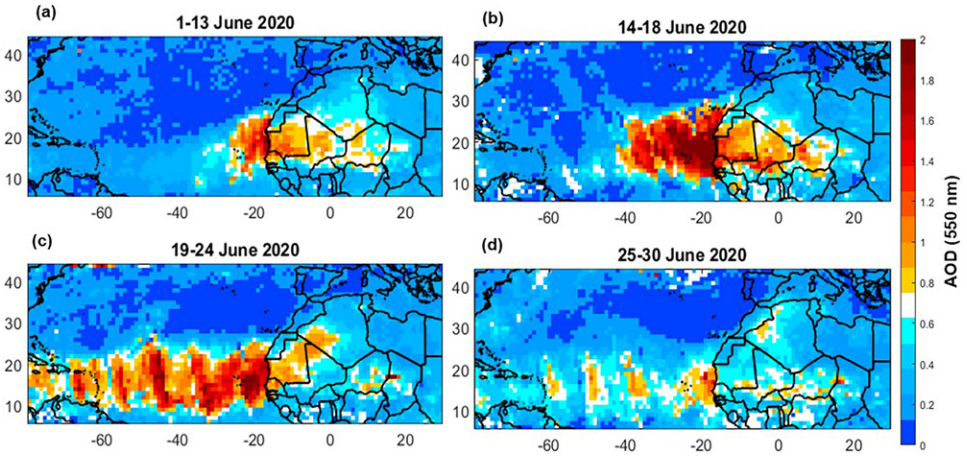

Fig. 5. Time-averaged MODIS AOD at 550 nm in the geographical domain 5°–45°N, 80°W–30°E for (a) 1–13 Jun 2020, (b) 14–18 Jun 2020, (c) 19–24 Jun 2020, and (d) 25–30 Jun 2020 (source: MODIS AOD data used in this work can be freely obtained at https://giovanni.gsfc.nasa.gov/giovanni/).

north anticyclonically and turns eastward across northern North Africa. Near ground (925 hPa), a negative NAFDI phase shows an anticyclonic airmass circulation over the western Sahara (Fig. 4c).

During the 1–13 June period, we observed strong heating over the Algerian–Libyan border and strong cooling on the coasts of Morocco and western Sahara, resulting in an east phase of the SHL corresponding to a negative phase of NAFDI (Cuevas et al. 2017), consistent with our observations.

2) NAFDI positive phase. According to the description of the daily evolution of dust plumes in section 3a and recognizing that the meteorological patterns in the positive NAFDI period are not as homogeneous as those found in the negative phase, we have subdivided the analysis of this second phase into three subperiods: 14–18, 19–24, and 25–30 June (Fig. 6).

From 14 June, under the positive phase of NAFDI, the geopotential height pattern at 700 hPa (Fig. 6a) changes radically. As described by Cuevas et al. (2017), the NASH and the North African high at 700 hPa merge into a single large anticyclone, with its southern flank favoring effective airmass transport from Africa to America (Fig. 6d).

Coinciding with the change of NAFDI to a positive phase, an increase in thunderstorm activity is observed over the SHE in RGB EUMETSAT imagery, causing two strong haboobs on 14 and 15 June in the SHE. These haboobs did not affect the SSS because the wind flow over the West Africa (WA) region was already cyclonic, thus explaining the AOD peaks observed only in the SHE (Fig. 3b).

The deep and persistent trough observed in the eastern Atlantic rapidly retracted on 14 June, with the drastic change to a positive phase of NAFDI. However, it did not completely disappear until 18 June (Figs. 6a,b). During these 5 days, the contraction of the trough, which practically became a cut-off low, favored easterly winds over the subtropical Atlantic (Figs. 6d,g). However, it affected the North African high, flattening it on its northern flank and displacing it southward (Fig. 6a). The negative NAFDIDI values registered on 18 and 19 June reflected this anomaly. During these days, the cut-off low was positioned over the northern half of Morocco, dramatically reducing the 700-hPa geopotential height values of the subtropical region of the dipole, resulting in negative NAFDIDI values on 18 and 19 June (Fig. 3a).

Given the interaction between the North African high and the SHL (Chen 2005), it is expected that the anomalies recorded in the former were transmitted to the latter, as is the case when registering negative values of the SHLLSI (on 16, 17, and 18 June). During an undisturbed

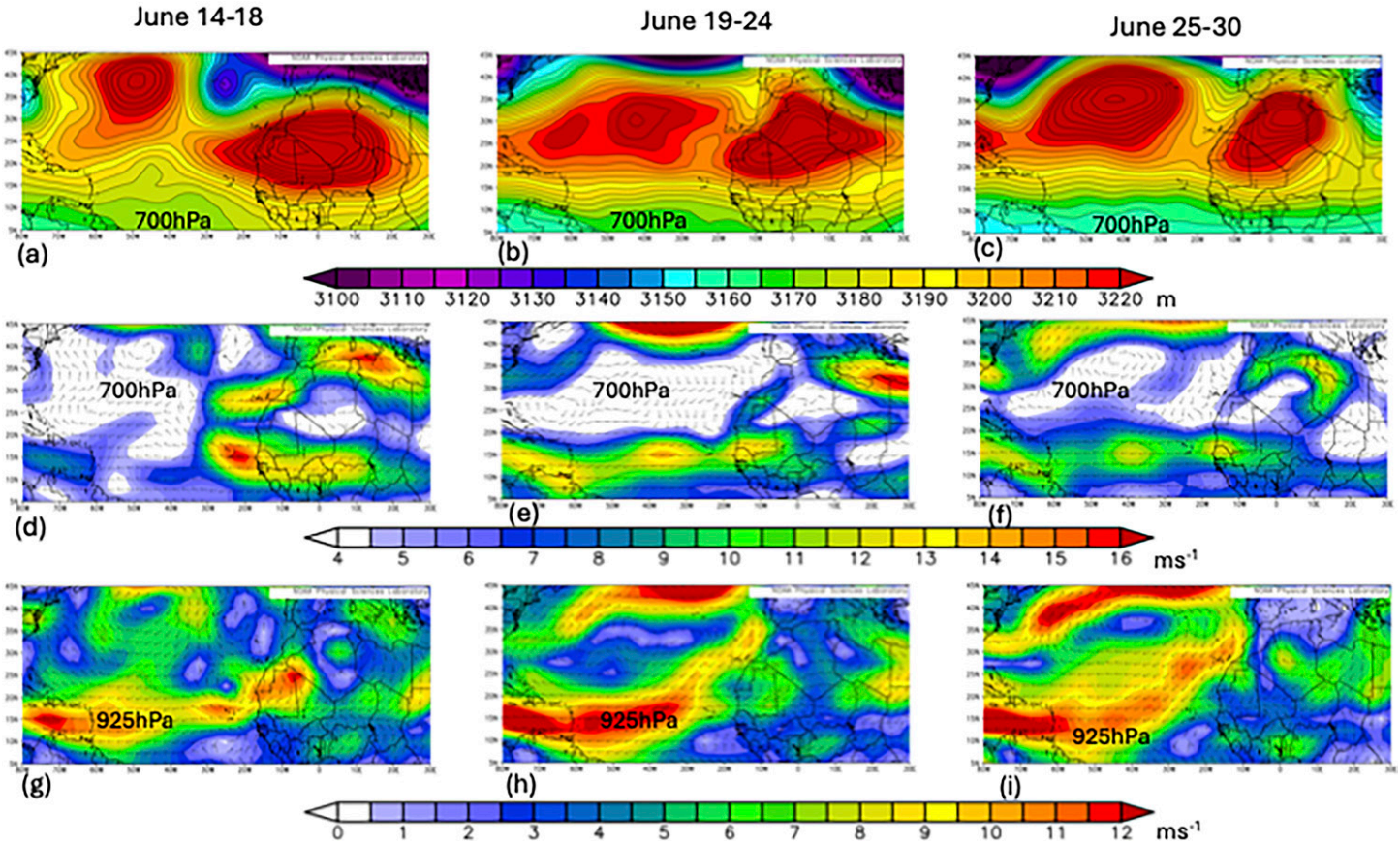

FIG. 6. Time-averaged geopotential height at 700 hPa (m) for (a) 14–18 Jun, (b) 19–24 Jun, and (c) 25–30 Jun; time-averaged vector wind at 700 hPa (m s^{-1}) for (d) 14–18 Jun, (e) 19–24 Jun, and (f) 25–30 Jun; time-averaged vector wind at 925 hPa (m s^{-1}) for (g) 14–18 Jun, (h) 19–24 Jun, and (i) 25–30 Jun, in the geographical domain 5°–45°N, 80°W–30°E, under the positive NAFDI phase (source: NCEP/NCAR reanalysis).

positive NAFDI phase, a strong warming is observed near the surface and centered on Morocco's South Atlantic coast (~30°N) resulting in a western SHL (Cuevas et al. 2017). However, during the anomalous period 14–18 June, the greatest increase in temperature at 925 hPa (~+4°C) was registered much further southeast, just north of the southern border of Mauritania (~20°N), causing the SHL to shift to the SE, far from its usual position under positive values of SHLLSI. From 16 to 18 June, the anomalous warming region, which was elongated to the east, affected the eastern point (20°N, 7.5°E) used to calculate the SHLLSI (Cuevas et al. 2017), which registered a higher temperature of that of the western point (25°N, 12.5°W), resulting in erroneous negative SHLLSI values.

The anomalous position of the SHL located so far south (20°N) played a crucial role in two atmospheric processes that lifted vast amounts of dust during 14–18 June 2020: 1) perturbation of the nearby ITD, triggering MCSs in both the SHE and SSS (RGB EUMETSAT animations, see SA1). 2) Creation of a huge geopotential height gradient at its northwest (NW), resulting in sustained northeastern (NE) strong ground-level winds (>12 m s^{-1}) (Fig. 6g), peaking on 16 and 17 June (>15 m s^{-1}) over the SSS. The wind speeds registered during the 15–18 June 2020 period were between 5 and 12 m s^{-1} higher than the climatological values (1991–2020 NCEP/NCAR reanalysis). Francis et al. (2020) also reported strong surface winds in a similar period before 18 June in a geographic domain (19°–30°N; 20°W–0°) close to the SSS.

These two atmospheric processes resulted in an extraordinary transport of dust (Fig. 5b) to the GCB until 18 June. Both the SSS and SHE showed the second highest AOD of June 2020, 0.7 and 0.9, respectively (Fig. 3b).

Simultaneously, the circulation changed at 700 hPa, the altitude where the maximum transport of Saharan dust toward the Atlantic takes place in summer (Rodríguez et al. 2015; Barreto et al. 2022). On 13 June, the flow turned northward a few kilometers from the coast, gradually made that turn more and more to the west, becoming completely zonal on 18 June. This gradual change in the wind at 700 hPa (Fig. 6d) caused dust to accumulate over the coastal region, where the dust plume would emerge over the ocean on 18 June (Fig. 5b), as reported by Yu et al. (2021). On 18 June, Godzilla (Fig. 5b) emerged over the Atlantic.

Moreover, dust lifted by MCSs is also observed in the SSS but with lower intensity than that observed in the previous period (RGB EUMETSAT imagery, see SA1). As a result, the average AOD of the SSS is higher than that of the SHE (Fig. 3b). Therefore, the SSS seems to be the main contributor to the transport of dust to the GCB in this period and also to the appearance of a second dust plume on the 24th (Fig. S5), which was much weaker than the first (Fig. 5c). Finally, in the period 25–30 June, the dust mobilized in the SSS and SHE decreased significantly (Fig. 3b), resulting in a very weakened dust plume moving toward the Caribbean (Fig. 5d), thus ending the life of Godzilla.

During the two dust plumes of June 2020, negative zonal wind anomalies were observed in the African easterly jet (AEJ) (not shown here), also reported by Francis et al. (2020) and Pu and Jin (2021). These features are consistent with a more effective transport of African air masses to the Caribbean (e.g., Kramer et al. 2020a).

c. Altitude of the African dust transport over the Caribbean. The vertical structure of the African dust plume can be measured using spaceborne and ground-based lidar. Yu et al. (2021) examined the evolution of CALIOP aerosol extinction profiles by following the dust plumes across the Atlantic. They found that the top of the Godzilla plume on 17–18 June 2020 reached 6–8 km near West Africa, higher than the climatological altitude of summertime extreme dust events (i.e., ca. 5 km; Huang et al. 2010). The top descended to about 4 km when the plume entered the eastern Caribbean on 23–24 June and subsequently into the United States over Texas on 27 June. CALIOP also suggests that the dust in the marine boundary layer had become mixed with marine aerosols by the time it reached the Caribbean. The CALIOP-inferred westward traveling speed (1000 km day^{-1}) of the Godzilla plume is consistent with the climatology of summer extreme dust events derived from MODIS/*Aqua* 2003–07 observations (Huang et al. 2010).

The Cloud-Observing Radar and Lidar (CORAL) (Stevens et al. 2016) based on Barbados (13.163°N, 59.429°W) corroborates with high temporal resolution the CALIOP-inferred altitude distribution of the aerosol layer and provides additional detail on how the dust mixes into the boundary layer (Fig. 7). The depolarization ratio serves as a measure of the asphericity of aerosol particles. Because dust particles are largely aspherical, CORAL can distinguish them from the more spherical sea-spray aerosol. Due to a residual polarization impurity in the sounding laser beam in the CORAL lidar, which was confirmed for the period of interest, the absolute values of the depolarization ratio were significantly biased toward low numbers. Nevertheless, even with this underestimation, we could perform qualitative analysis with CORAL to distinguish between dust and sea spray. Figure 7 indicates the dust layer reaches up to 3.5–4 km above Barbados, with most of the dust residing in the SAL directly above the trade-wind inversion at approximately 1.5 km as previously observed (Prospero and Carlson 1972; Prospero et al. 2021). A meteorological sounding made at 1200 UTC at the nearby airport yields a classic SAL with a sharp inversion at 1.5 km and a second at about 4.0 km with an isentropic layer between the two altitudes. These features exactly match the altitude distribution of the CORAL aerosol profile (Fig. S7a). In places, buoyant plumes from below the trade-wind inversion appear to have penetrated the base of the dust layer and subsequently

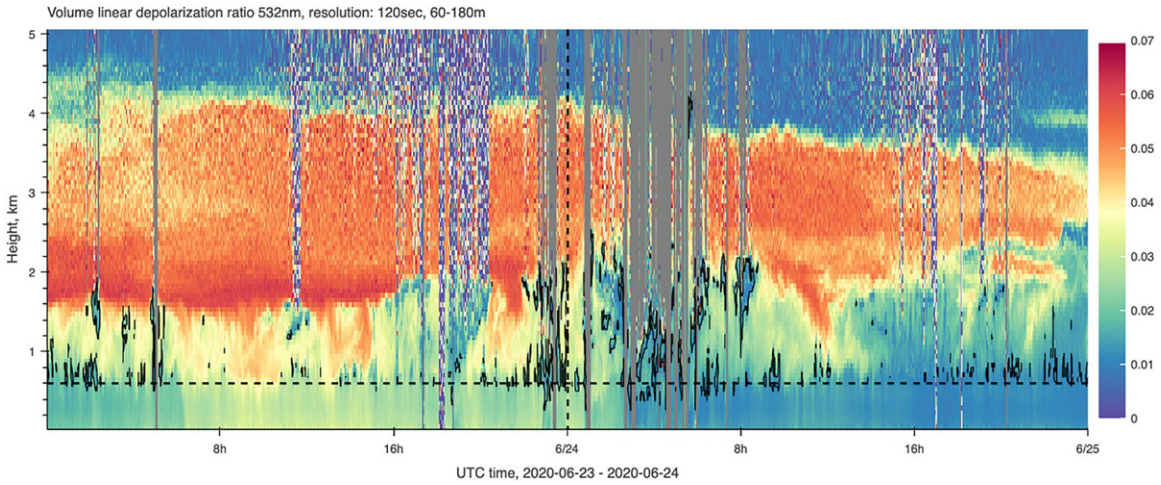

Fig. 7. Evolution of the Godzilla dust plume above BAR (13.163°N, –59.429°W) during 23–24 Jun 2020, based on measurements of volume depolarization ratio using the CORAL lidar. The days with the maximum aerosol loading measured with filters at Ragged Point are associated with a very-high-volume depolarization ratio. Dust, having more aspherical aspect ratios, will produce higher values of the depolarization ratio, with all other properties remaining unchanged. Black contours indicate clouds. The dashed vertical line indicates 0000 UTC 24 Jun. The dashed horizontal line indicates the approximate cloud base (estimated to be at 600 m). The plumes seen descending from the SAL base suggest that dust is actively transferred from the SAL to the marine boundary layer air by convective mixing processes.

entrained dust, carrying it downward to the surface as seen on 23 June. The transfer of dust from the SAL into the boundary layer by convective erosion of the SAL base inversion was first noted in extensive aircraft flights in the Barbados region in 1969 (Carlson and Prospero 1972). Many studies (e.g., Castellanos et al. 2024) suggest that the dust is well mixed in the vertical in SAL due partly to convective mixing driven in part by dust radiative heating within the dust layer.

After entering the Caribbean, the plume moved westward. A portion of the plume subsequently turned anticyclonically, heading north over the Gulf of Mexico into Texas, and then turned east, eventually appearing over the Florida Panhandle on 25 June (Yu et al. 2021). The plume continued its anticyclonic trek, reaching Miami (26°N, 80°W) on 26 June, where it was detected by a micropulse lidar with depolarization capability (Fig. 8; Delgadillo et al. 2018). This pattern is common in June (Kramer et al. 2020a) and reflects the effects of the westward extension of the NASH also shown in Yu et al. (2021). The top of the plume above Miami remained near 4 km on 28 June, descending to 3 km after 29 June due to the increasing influence of the subsidence associated with the NASH. These altitudes are typical of SAL dust layers over Miami (Kramer et al. 2020b). Notably, the dust layer remained coherent and elevated during its transit over the Gulf of Mexico and the southern and southeast United States, a period of approximately 5 days.

It is significant that at Miami, the extinction values are associated with large volume-depolarization ratios that attain values typical for dust emitted near sources [>0.3; see comparisons to other dust events over Miami in Kramer et al. (2020b)] (Fig. 8 and Fig. S7b). This suggests that there was little mixing of SAL air with air from the northern Atlantic or even from the southeastern United States. Apparently, the dusty African air mass displaces the ambient air during its passage over land rather than mixing with it. The dusty air itself remained well mixed in the vertical, especially near the top of the SAL, also evident in Miami lidar soundings, further indicating an ability for the dust plume to retain some of its original SAL features after 10 days of transport from sources deep within North Africa. Over Africa, haboob-type dust storms can generate deep dust columns with enhanced moisture at the upper altitudes in the dust layer compared to a nondusty atmosphere and thereby

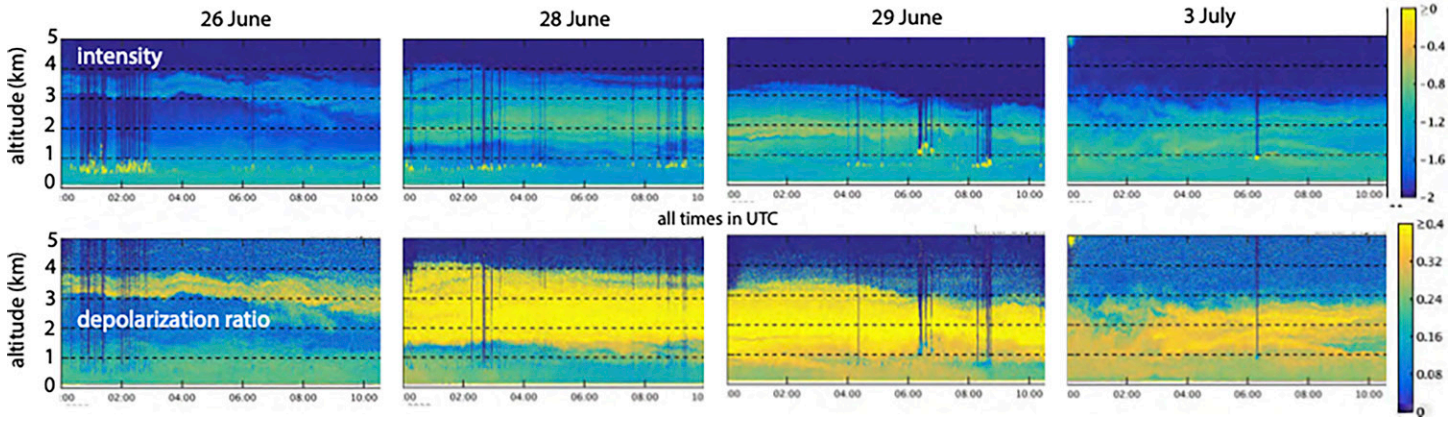

Fig. 8. Evolution of (upper) the backscattered intensity record and (lower) the volume depolarization ratio above Miami, from 26 Jun through 3 Jul 2020, as observed by a micropulse lidar. The logarithmic color scales should be interpreted qualitatively. The upper panels show increasing amounts of aerosol being advected over Miami with time. The lower panels show that the SAL subsides as the dust event moves through the region. The volume depolarization ratios are relatively large, which could be interpreted to mean that the aerosol is dominated by aspherical particles (e.g., mineral dust) that overwhelm other types of aerosols that are more spherical, most likely sea salt.

increase layer-top cooling through longwave radiation (Ryder 2021; Barreto et al. 2022). The sinking of the cool air induces turbulent mixing in the SAL, which can help maintain its integrity. The minimal mixing observed over Miami does not contradict the CALIOP results of dust well mixed in the marine boundary layer. These results most likely reflect that Puerto Rico and Miami were affected by different parts of the dust plume.

d. How well were the events predicted by dust forecast models? Numerous research and operational modeling systems have provided dust forecasts for early warning over the GCB region, including the nine global forecasts that participated in the International Cooperative for Aerosol Prediction (ICAP) (Xian et al. 2019). Additionally, there are at least three regional dust forecasting systems routinely operated in this region including (i) the Caribbean Institute for Meteorology and Hydrology maintains WRF-Chem; (ii) the U.S. National Weather Service (NWS) National Air Quality Forecast Capability (NAQFC) which, as of 2024, covers the North America and part of the Central America, including the Puerto Rico region; and (iii) the NWS San Juan–Puerto Rico Field Office forecast operations of dust and total PM_{10} and $PM_{2.5}$ over the Caribbean region to support authorities in managing air quality and health risks associated with trans-Atlantic–Africa dust in small island states (SISs) (Tong et al. 2023). Here, we utilize simulations from WRF-Chem and GEOS, which are two of the most commonly used dust forecast models for the GCB.

1) WRF-Chem forecast. The WRF-Chem model (initialized 0000 UTC 20 June) forecast that moderate-to-high AOD and dust surface concentrations would affect the eastern GCB beginning around 21 June (Fig. 9a). WRF-Chem predicted that the most intense dust plume would reach the eastern GCB by 23 June based on the model AOD and reach the western GCB by 25 June. The WRF-Chem surface dust forecast differs from the AOD forecast; in that, the former shows substantial dust in surface air that arrives well in advance of the AOD dust "front" on 21 June (Fig. 9a). Indeed, surface measurements show substantial increases of aerosol at some sites as early as 19 June (e.g., Martinique and Guadeloupe, see below).

WRF-Chem predicted peak surface dust concentrations at >400 $\mu g\ m^{-3}$ over a large area of the region and peak AOD at >1.5 in several areas. This forecast (Fig. 9b) shows an extremely large plume that, on 25 June, encompassed the entire GCB, with surface dust concentrations exceeding 400 $\mu g\ m^{-3}$ in the plume core. WRF-Chem predicted AOD to be around 0.9 at the periphery of the plume and 1.5 in the core (Fig. 9a).

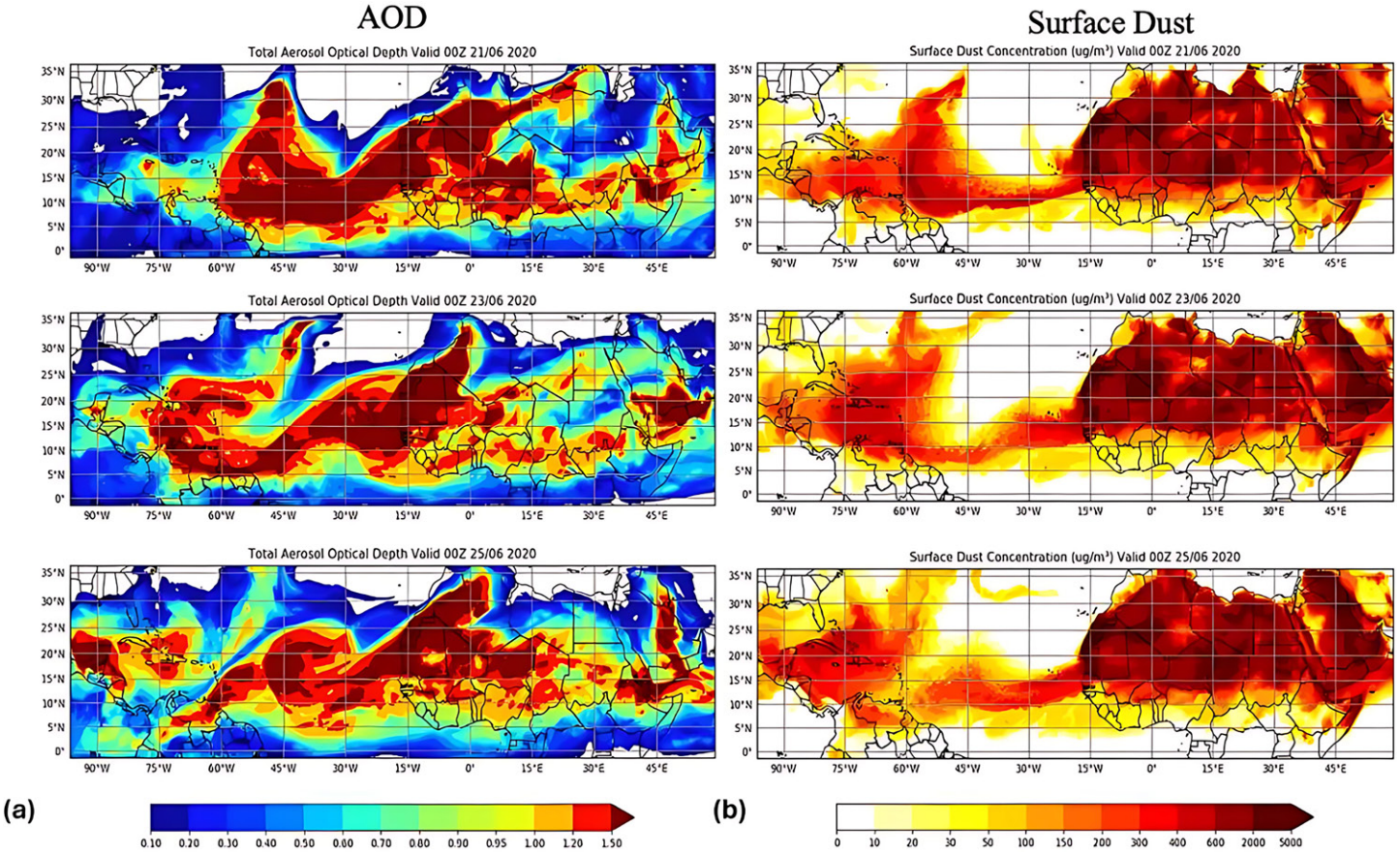

Fig. 9. WRF-Chem prediction of (a) AOD and (b) surface dust concentration initialized at 0000 UTC 20 Jun 2020 and valid for (top) 0000 UTC 21 Jun 2020, (middle) 0000 UTC 23 Jun 2020, and (bottom) 0000 UTC 25 Jun 2020, respectively.

2) NASA GEOS MODEL. Figure 10a shows the progression of daily GEOS forecasts of the total AOD at CSJ, Puerto Rico, beginning on 13 June. Each trace shows the 10-day forecast initialized from 0000 UTC on the indicated day. Note the very low total AOD forecast before 18 June. However, there are hints of a greatly increased AOD as was later observed on 22–23 June. The predicted AOD increased as the forecast initialization time approached the peak on 23 June. The highlighted 18 June forecast in Fig. 10a shows a moderate total AOD ≈ 1.0 spanning 22–23 June and a pronounced peak on 20 June, 2 days before the arrival of the major event. As the forecast time approached the time of the event (lighter yellow colors), the AOD forecast values increased. This improving agreement trend demonstrates the value of the aerosol data assimilation used in GEOS. Later forecasts reduced the magnitude of the peak on 20 June but progressively increased so that on 22 June, the forecast is close to observations (Fig. 10c), as, for example, the forecasts initialized on 20 June. In addition, the forecast shows the arrival of a minor dust event on 26–28 June.

In contrast, WRF-Chem (Fig. 10b, also highlighting the forecast initialized on 18 June) predicted a higher peak AOD, about 1.6, for the period 22–24 June. Also, the predicted AODs between 27 and 28 June were a factor of 3 higher than in GEOS. WRF-Chem does not use data assimilation. But overall, there is greater consistency in the WRF-Chem forecasts leading up to the dust event than in the GEOS forecasts. In Fig. 10c, we also show the daily mean AOD measured at the CSJ–PR as part of AERONET (Holben et al. 1998) and over the same period as in Fig. 10a. Figure 10d shows the daily means obtained in all eight spectral channels. The AODs are nearly identical except at 1640 nm. The lack of spectral variability (i.e., neutral extinction with an Ångström exponent near zero) is an identifying characteristic of atmospheric mineral dust. The lack of spectral variability in the AOD magnitude at shorter wavelengths is characteristic of coarse atmospheric dust particles and is commonly observed in AOD measurements in the

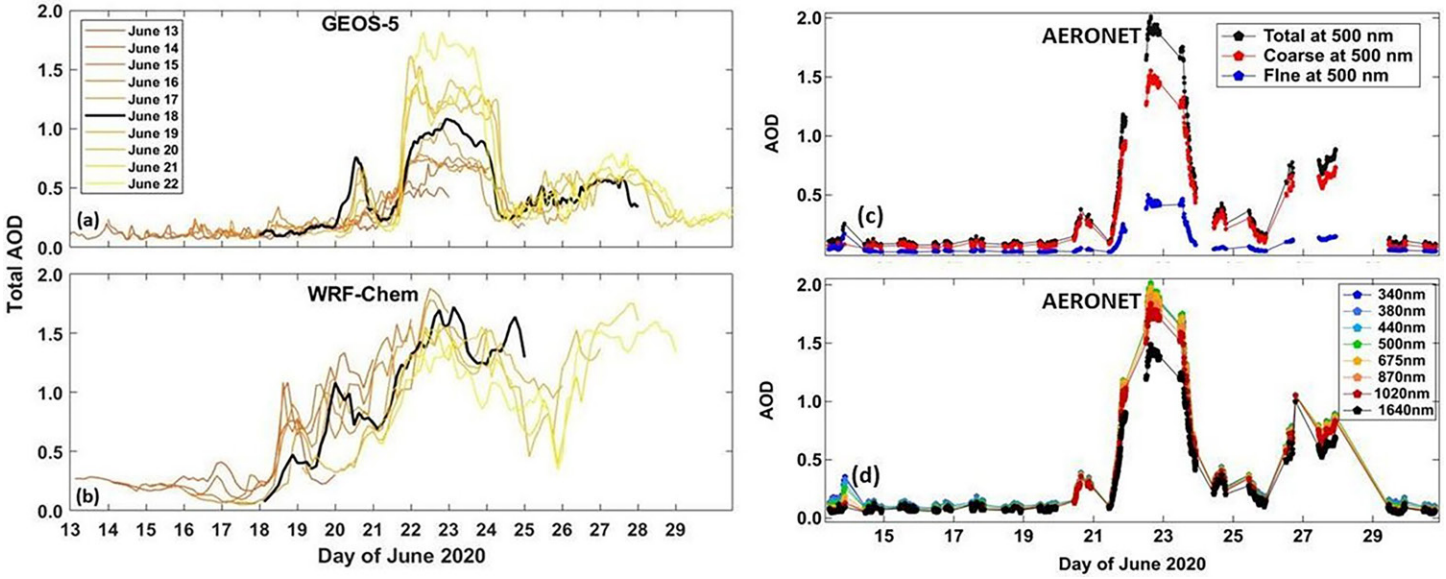

FIG. 10. (a) GEOS forecast total AOD and (b) WRF-Chem forecast total AOD at CSJ–PR, color coded by the forecast initialization time. The 0000 UTC 18 Jun forecast is highlighted by the thick black line. (c) CSJ–PR AERONET total coarse and fine AOD and (d) CSJ–PR AERONET daily mean AOD obtained in all 8 spectral channels (340, 380, 440, 500, 675, 870, 1020, and 1640 nm).

GCB in summer. Figure 10c shows the fine and coarse AOD values which are calculated based on the extinction at 440 and 870 nm. When Godzilla reached CSJ, the coarse particle fraction increased greatly relative to the fine particle fraction, a change that we would expect for the arrival of a relatively coarse aerosol like soil dust. In summary, as the forecast initialization time approaches the verification date (22–23 June), GEOS does a better job of predicting the observed sharp rise in dust AOD, but earlier than 20 June, the GEOS forecasts underestimate the observed peak while WRF-Chem more consistently forecasts the high peak AOD that was observed.

Comparisons of Figs. 9 and 11 suggest some explanation for differences between the GEOS and WRF-Chem simulations. On 23 June, both WRF-Chem and GEOS predicted significant amounts of dust over the Caribbean, with WRF-Chem predicting an overall higher (>1.5) total AOD than GEOS (~1.2). It also shows much higher AOD over the Saharan desert source region, with a regional average AOD > 1.5, while GEOS yields AOD values mostly <1. Comparisons of simulated surface mass concentrations are also illustrative, with WRF-Chem showing mass concentrations >400 μg m^{-3} (Fig. 9b) over the Caribbean on 23 June, while GEOS is closer to 200 μg m^{-3} (Fig. S8). While the regional AOD only differs by about 50%, the surface concentrations differ by more than a factor of 2. This suggests either a difference in the simulated vertical distributions of dust, a relatively larger coarse mode contribution to total dust in WRF-Chem, or the method used to calculate AOD from dust mass loading in WRF-Chem (i.e., more massive but less optically efficient particles).

Aerosol forecast models, even those using data assimilation, are mostly constrained by the total column AOD (Xian et al. 2019); aerosol emissions, removal, speciation, particle properties, and vertical distribution are model-dependent prognostic variables. As seen by the GEOS and WRF-Chem results, there can be considerable differences among models. While GEOS predicted the sharp rise in AOD observed with AERONET, it underestimated the magnitude. In this study, WRF-Chem did not use data assimilation, and, consequently, its higher forecast AOD is because of other model parameterizations. CALIMA in situ observations of mass and particle size could provide constraints on aerosol transport models, for example, by refining model assumptions of dust particle size distribution and mass-to-extinction relationships implied in model optical properties (e.g., Castellanos et al. 2024). It is important to stress that the AOD assimilation applies to the total AOD. The partitioning of AOD across species is a function of the model algorithm and so is a source of uncertainty.

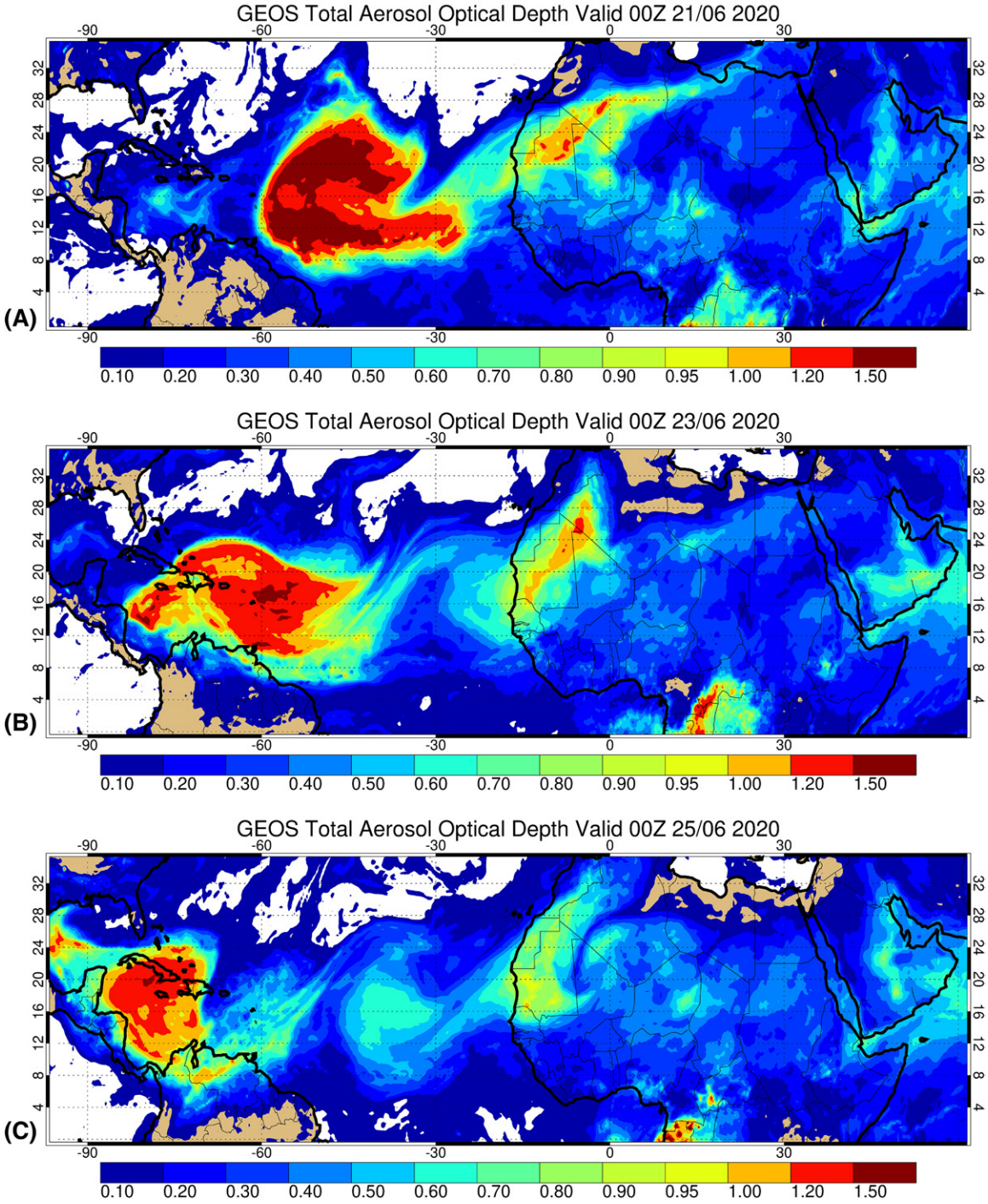

Fig. 11. Forecast total AOD from the GEOS at 0000 UTC 20 Jun 2020, forecast for each of (a) 0000 UTC 21 Jun 2020, (b) 0000 UTC 23 Jun 2020, and (c) 0000 UTC 25 Jun 2020.

e. Godzilla's impact on air quality. African dust transport can lead to a reduction in air quality near the sources in Africa as well as after long-range transport to the GCB (Prospero et al. 2001; Prospero and Mayol-Bracero 2013; Raga et al. 2021). This was clearly seen during Godzilla (Pu and Jin 2021; Yu et al. 2021; Mehra et al. 2023). Figure 12 shows PM_{10} mass concentrations at Puerto Rico from 19 to 29 June. What we refer to as the first dust pulse of the Godzilla event is represented by peaks 1–5 with the highest concentrations occurring on 21–24 June (peaks 2 and 3 in Fig. 12). A second major pulse was observed on 26–29 June (peak 6 in Fig. 12).

Surface visibility was greatly reduced in San Juan, Puerto Rico, on 22–23 June as shown in measurements (Fig. 12) and in photographs (Fig. 13). The reduction is consistent with

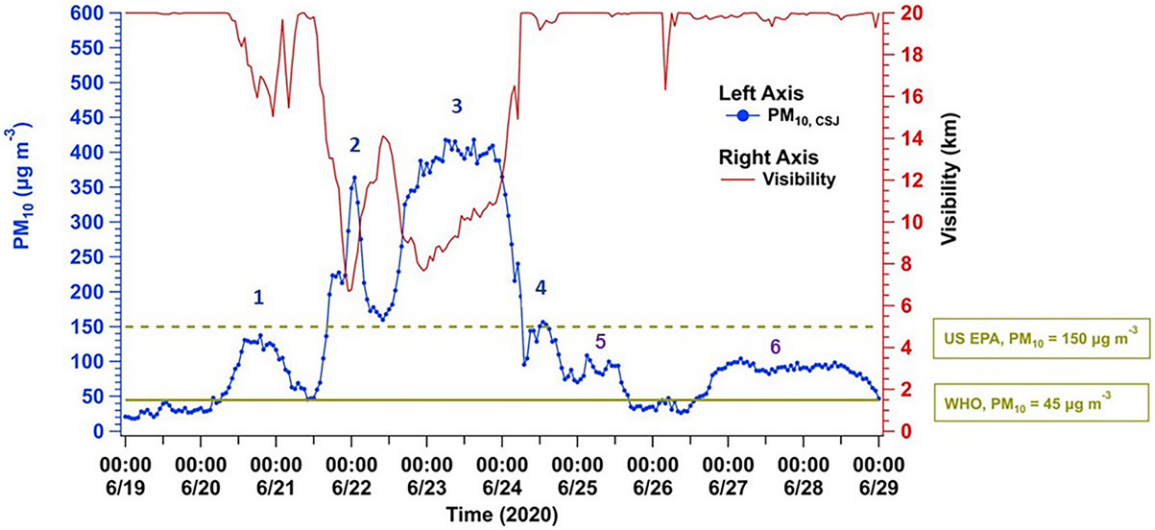

Fig. 12. PR (CSJ–PR) PM_{10} mass concentrations (primary *y* axis) and visibility (secondary *y* axis) from 19 to 29 Jun. The first dust pulse (Godzilla) is represented by peaks 1–5. Peak 6 represents a second dust pulse. The gold horizontal lines show the U.S. EPA and WHO 24-h PM_{10} guidelines.

the empirical relationship between PM_{10} and horizontal visibility (Camino et al. 2015). The meteorological soundings at San Juan (Figs. S7c,d) reveal the presence of a classical SAL structure with an elevated dry isentropic layer. The increased surface-level dust concentrations are believed to be largely the result of downmixing from the SAL, a feature also seen in lidar observations at Miami and Barbados (Figs. 7 and 8) during Godzilla. At the peak of the event, when PM_{10} reached its maximum, the visibility decreased to 7–8 km (Fig. 12), the skies went dark, visibility was reduced, and air quality was degraded. The series of events affected the region for about 15 days (18 June–1 July 2020).

Figure 14 shows the time series of PM_{10} and $PM_{2.5}$ in the GCB. Godzilla was observed at most GCB stations but not at CAY which was in the ITCZ as is typical for this time of year. Similarly, Trinidad was located south of the main plume. Figure S9 shows the Lagrangian path of the Godzilla plume based on the airmass back trajectories [Hybrid Single-Particle Lagrangian Integrated Trajectory model (HYSPLIT); Stein et al. 2015]. The 7000-km-long Godzilla path and the timing of the advance of the dust front are consistent with the PM record shown in the time series plots of PM_{10} (Fig. 14a) and $PM_{2.5}$ (Fig. 14b).

Table 2 presents the observed mean PM_{10} and $PM_{2.5}$ mass concentrations measured during Godzilla in the GCB and the guideline exceedance factor: the ratio of those concentrations

Fig. 13. Photos taken in CSJ, PR, (left) on 29 Apr before the Godzilla event and (right) on 22 Jun during the event (credit: Olga Mayol-Bracero).

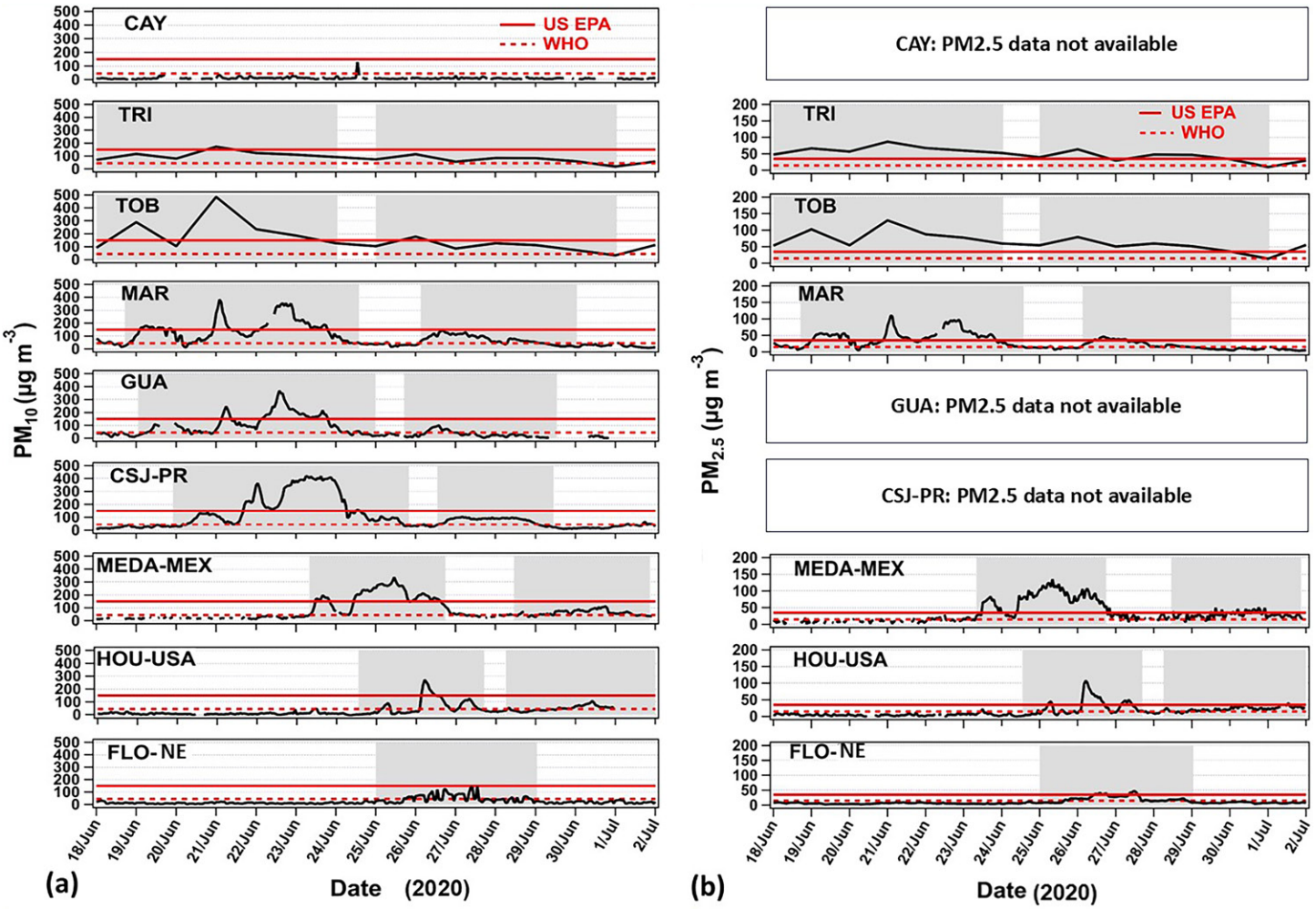

FIG. 14. (top–bottom) Lagrangian path of the Godzilla dust event represented by (a) PM_{10} and (b) $PM_{2.5}$ mass concentrations observed at the GCB sites. The gray-shaded region in the background represents the duration of the two main dust events at the different stations. The red horizontal lines refer to the 24-h PM_{10} and $PM_{2.5}$ guidelines of EPA (solid line) and WHO (dashed line).

to the WHO and U.S. EPA guidelines. Most stations exceeded both the WHO and U.S. EPA PM_{10} 24- and $PM_{2.5}$ guidelines. At times, they were almost twice the U.S. EPA guidelines. At Tobago, they were 4 times and 5 times stricter WHO guidelines for PM_{10} and $PM_{2.5}$, respectively. At Martinique and Puerto Rico, the period of exceedances lasted 9–10 contiguous days. Thus, Godzilla constituted a major existential threat to public health over a huge area. For example, based on the air quality indexes (AQIs) associated with the observed PM_{10} concentrations, Puerto Rico experienced "unhealthy for sensitive groups" or "hazardous" conditions over 3 days based on U.S. EPA guidelines and over 9 days according to WHO guidelines.

The ratio of $PM_{2.5}$ to PM_{10} mass concentration ($PM_{2.5}/PM_{10}$) was remarkably constant during Godzilla (Fig. 15) in the GCB region. At the peak of Godzilla (22 and 23 June at MAR) when PM_{10} was at moderate-to-high values, the $PM_{2.5}/PM_{10}$ was low, about 0.3, when PM_{10} was at moderate-to-high values showing that the event was dominated by coarse particles. The ratio was quasi constant which suggests that the dust was well mixed across the impacted region and may also indicate that there is little variation in the dust size distribution following transport consistent with findings by Denjean et al. (2016). The Martinique measurements are most representative of the Godzilla dust properties because the site is located on the east coast of the island, and it is minimally impacted by local or regional sources. However, at the height of the event, a somewhat higher ratio (about 0.4) was measured at sites where there are substantial local pollutant aerosol sources,

Table 2. Duration (number of days above the WHO PM guidelines) that Godzilla dust plume impacted the regional air quality at locations in the GCB. Shown are the observed daily mean mass concentrations (PM_{10} and $PM_{2.5}$) and exceedance factors (U.S. EPA and WHO) of the Godzilla dust plume during 18 Jun–21 Jul 2020.

	CAY	TRI	TOB	MAR	GUA	CSJ–PR	MEDA_mEX	HOU–USA	FLO
PM_{10} (U.S. EPA: 150 $\mu g\ m^{-3}$)									
Days	0	1	5	4	2	3	3	0	0
Mean ($\mu g\ m^{-3}$)	0	173	275	192	196	274	185	0	0
Factor	0	1	2	1	1	2	1	0	0
PM_{10} (WHO: 45 $\mu g\ m^{-3}$)									
Days	0	14	14	10	6	9	6	3	2
Mean ($\mu g\ m^{-3}$)	0	93	166	120	116	147	133	86	66
Factor	0	2	4	3	3	3	3	2	1
$PM_{2.5}$ (U.S. EPA: 35 $\mu g\ m^{-3}$)									
Days	—	11	14	4	—	—	5	1	0
Mean ($\mu g\ m^{-3}$)	—	58	68	56	—	—	62	49	0
Factor	—	2	2	2	—	—	2	1	0
$PM_{2.5}$ (WHO: 15 $\mu g\ m^{-3}$)									
Days	—	14	14	6	—	—	7	4	2
Mean ($\mu g\ m^{-3}$)	—	52	68	48	—	—	52	32	29
Factor	—	3	5	3	—	—	3	2	2

e.g., Houston and Mexico (HOU–USA and MEDA–MEX, Fig. 15). At these sites, the dispersion of the ratio at lower PM concentrations is evidence of local source impacts. It is notable that during Godzilla, $PM_{2.5}$ increased along with PM_{10}. Thus, dust $PM_{2.5}$ is a significant factor in terms of air quality concerns.

In Puerto Rico at CSJ, PM_1 and PM_{10} aerosol scattering and absorption were continuously measured in June 2020 using an integrating nephelometer and a CLAP. The dominance of coarse particles in Godzilla is evident. When scattering and absorption coefficients were at maximum (Fig. 16a) during the peak of the event, the SAE was at its minimum with values close to zero (Fig. 16b), which is evidence of the dominance of coarse-mode particles.

f. Godzilla as a record breaker of in situ aerosol optical properties, AOD, PM, and dust surface concentrations.

1) In situ aerosol optical properties. Record levels of aerosol scattering and absorption were measured at CSJ–PR throughout the event (Fig. 16a). Scattering was a factor of 10 higher and absorption a factor of 8 higher relative to the long-term record at the site. The 15-yr daily mean PM_{10} scattering and absorption coefficients are 34.4 ± 23.6 and 1.3 ± 1.7 Mm^{-1}, respectively, while the maximum green wavelength scattering and absorption coefficients observed were 364 and 10 Mm^{-1}, respectively. The coincidence of the very low PM_1 and PM_{10} scattering Ångström parameters during the event highlights the very distinctive character of the African dust outbreak (Fig. 16b). The impact of the Godzilla dust plume on in situ aerosol optical properties was more nuanced at sites further from the main plume (e.g., at Houston, Illinois, and North Carolina; Mehra et al. 2023).

2) MODIS and MISR aerosol optical depth. MODIS and MISR have been measuring atmospheric aerosol properties since 2000. The top panel of Fig. S10 shows a time series of the daily mean MODIS AOD over the Caribbean, defined here as a box extending from 15°–25°N to 60°–80°W. The daily mean is derived from MODIS *Terra* and *Aqua* using the dark target and deep blue AOD retrievals over ocean and land, respectively. All *Terra* and *Aqua* MODIS level 2

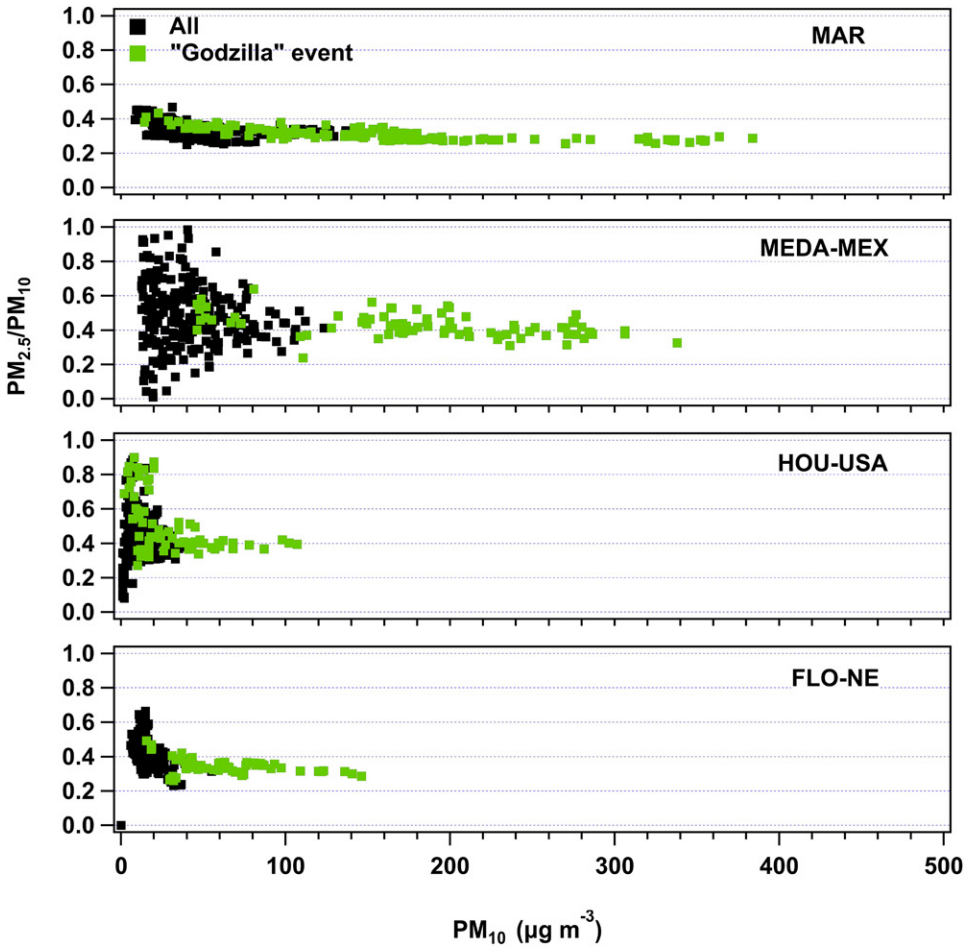

FIG. 15. Ratio of fine ($PM_{2.5}$) to coarse (PM_{10}) particle mass as a function of PM_{10} during the peak of the Godzilla dust event (green squares; e.g., 19–24 Jun at MAR) and for the whole period of study (black shading) between 18 Jun and 2 Jul, observed at MAR, MEDA–MEX, HOU–USA, and Florida-NE.

AOD retrievals from all MODIS granules that fall within the Caribbean latitude and longitude box on a particular day are simply averaged. For simplicity, we refer to this as the daily mean AOD, even though it is not a true daily mean since it only includes local times sampled by the MODIS instruments over our Caribbean box that are governed by the wide swath of MODIS and the 1030 and 1330 local solar time (LST) equator crossing time orbits of *Terra* and *Aqua*, respectively, during daylight. Godzilla stands out as a record high in the AOD time series, with a maximum mean AOD = 1.1 which occurred on 22 and 23 June 2020. The remaining panels in Fig. S10 show the monthly regional mean values of AOD segregated by aerosol size and shape measured by MISR: small (particle radii < 0.35 μm), medium (0.35–0.7 μm) and large (>0.7 μm) particles. The AOD data are also segregated into spherical and nonspherical particles. The MISR monthly regional mean values of total AOD attained a maximum value of 0.4 in June 2020, which is 0.12 higher than all other Junes in the MISR record. Figure S10 shows that this record-setting monthly regional mean AOD value is primarily driven by the AOD values of nonspherical medium and large-sized particles—a clear signature of desert dust (e.g., Dey and Di Girolamo 2010). The strong seasonal cycle of this dust signature stands out in the MISR record.

3) AERONET AEROSOL OPTICAL DEPTH. The daily average coarse mode AOD (NASA's AERONET data) measured at sites in the GCB from 2005 to 2020 is shown in Fig. S11a. During Godzilla, record high values were observed at most stations (e.g., BAR, GUA, CSJ–PR, and FLO-NW), with the 90th percentiles of the daily maximum coarse mode AOD significantly higher than for

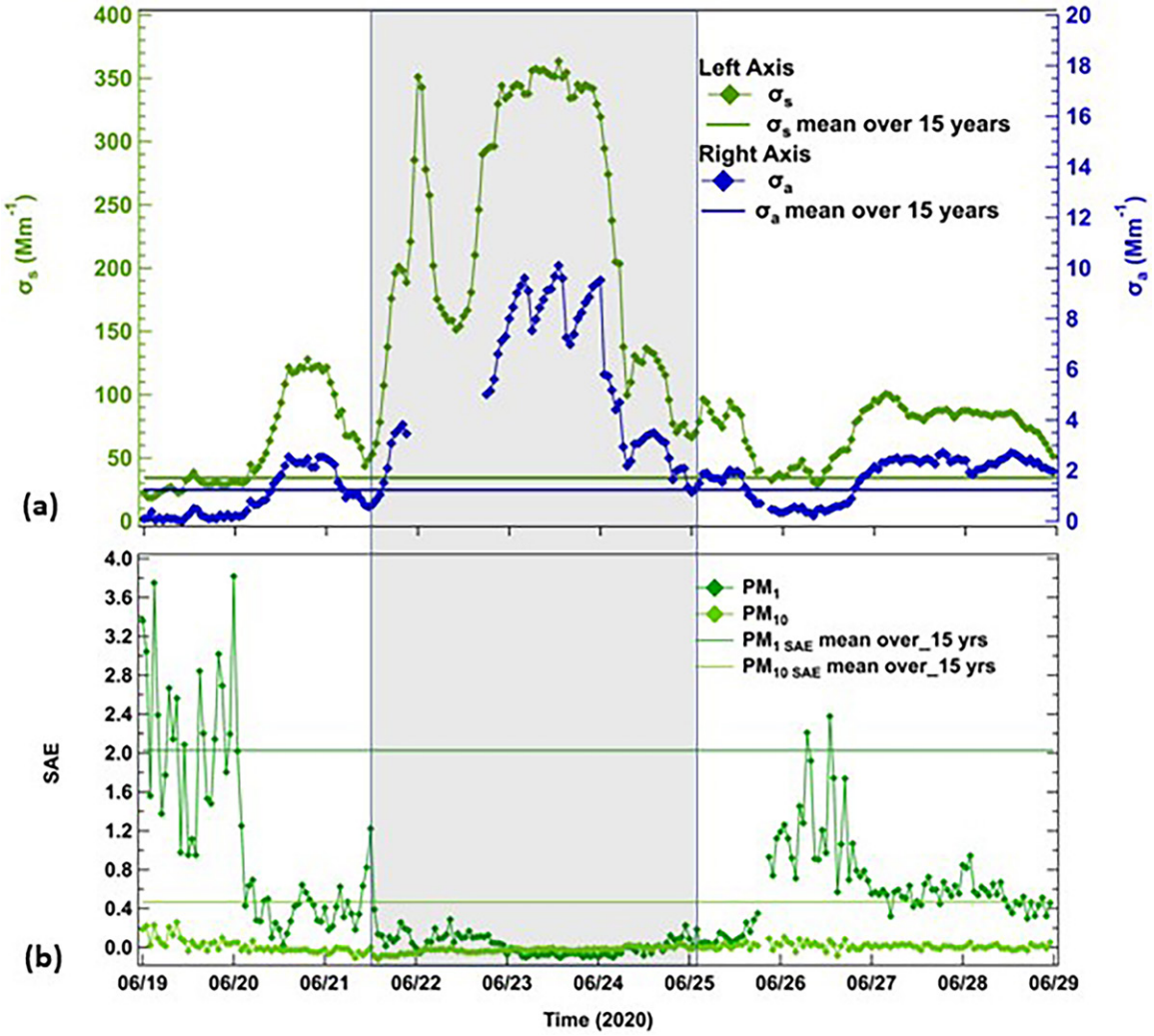

FIG. 16. (a) Aerosol optical data for PR. Scattering coefficient σ_s at 550 nm (primary *x* axis) and absorption coefficient σ_a at 528 nm (secondary *x* axis). The horizontal lines represent the 15-yr mean for scattering (green) and absorption (blue); (b) SAE (for PM_1 and PM_{10}). The horizontal lines represent the 15-yr mean of SAE for both size cuts. SAE is calculated using the 450- and 700-nm scattering measurements. The gray-shaded region represents the duration of the intense main dust event at CSJ–PR.

other years. In contrast, MIA–USA was only lightly impacted. Among these stations, BAR, GUA, CSJ–PR, and FLO-NW registered the highest daily maximum coarse mode AODs 1.2, 1.4, 1.5, and 1.05, respectively. CSJ–PR recorded the highest daily maximum coarse mode AOD (1.5) because the core of Godzilla passed over the site. Similar to coarse mode AODs, the 90th percentile of the fine mode daily maximum AODs also significantly increased during the passage of Godzilla (Fig. S11b). The fine mode AOD at BAR, GUA, CSJ–PR, MIA–USA, and FLO-NW were 0.38, 0.53, 0.43, 0.1, and 0.41, respectively. GUA and CSJ–PR recorded the highest daily maximum fine mode AODs based on their 12- and 14-yr historical records, respectively.

4) SURFACE PM CONCENTRATIONS. Godzilla yielded record values of PM_{10} and $PM_{2.5}$ in 2020 (Fig. S12). The highest daily mean PM_{10} values were recorded over Martinique (MAR), Puerto Rico (CAT–PR), Mexico (MEDA–MEX), and FLO-NE: 296, 453, 252, and 99 $\mu g\ m^{-3}$, respectively, as shown in Fig. S12a. The record of $PM_{2.5}$ is shown in Fig. S12b. At MAR, Puerto Rico (GUAY + MAYA–PR), MEDA–MEX, and FLO-NE, the highest concentrations of $PM_{2.5}$ were 71, 256, 101, and 45 $\mu g\ m^{-3}$, respectively. Puerto Rico experienced the highest PM_{10} and $PM_{2.5}$ measured in the last 17 years (2004–20) and the highest PM concentrations compared to all the locations considered in this study.

5) Dust surface concentrations. Total daily dust surface concentrations (DSCs) were measured using the TSP filter samples collected at BAR, CSJ–PR, and MIA–USA (Figs. 17a–c). During Godzilla, the highest dust concentrations at BAR and CSJ–PR were 161 and 393 μg m^{-3} on 20 and 22 June, respectively (Figs. 17a,b). Concurrently, BAR and CSJ–PR observed record values of AERONET AOD. These were 1.5 (21 June) and 2.0 (22 June) for BAR and CSJ–PR, respectively. In contrast, MIA–USA did not record high concentrations during the passage of the event and the surface-measured AOD showed only a small enhancement (0.4) on 28 June (Fig. 17c).

When the measured Godzilla DSCs are compared with the historical record at MIA–USA, CSJ–PR, and BAR, the highest concentration (393 μg m^{-3}) during the past 35 years was observed at CSJ–PR (Fig. 17). At BAR, DSC–TSP were high but not at the record levels that were observed at the height of the African drought in the 1980s (Prospero and Lamb 2003). At MIA–USA, DSC were quite modest, reflecting the fact that the core of the Godzilla transport path was located well to the south of Miami in the early stages of the event and to the north of Miami, over Georgia and north Florida, in the last days of the event. At BAR, the highest previous DSC (272 μg m^{-3}) was measured in April 1994 (Zuidema et al. 2019). At MIA–USA, the highest DSC (281 μg m^{-3}) was recorded in November 1985 at the peak of the drought in North Africa (Prospero and Lamb 2003), similar to the case with the BAR record.

4. Value of the integrative approach

Kahn et al. (2023) articulated a need for an integrative approach combining satellite observations, ground-based and airborne measurements, and aerosol and climate modeling to

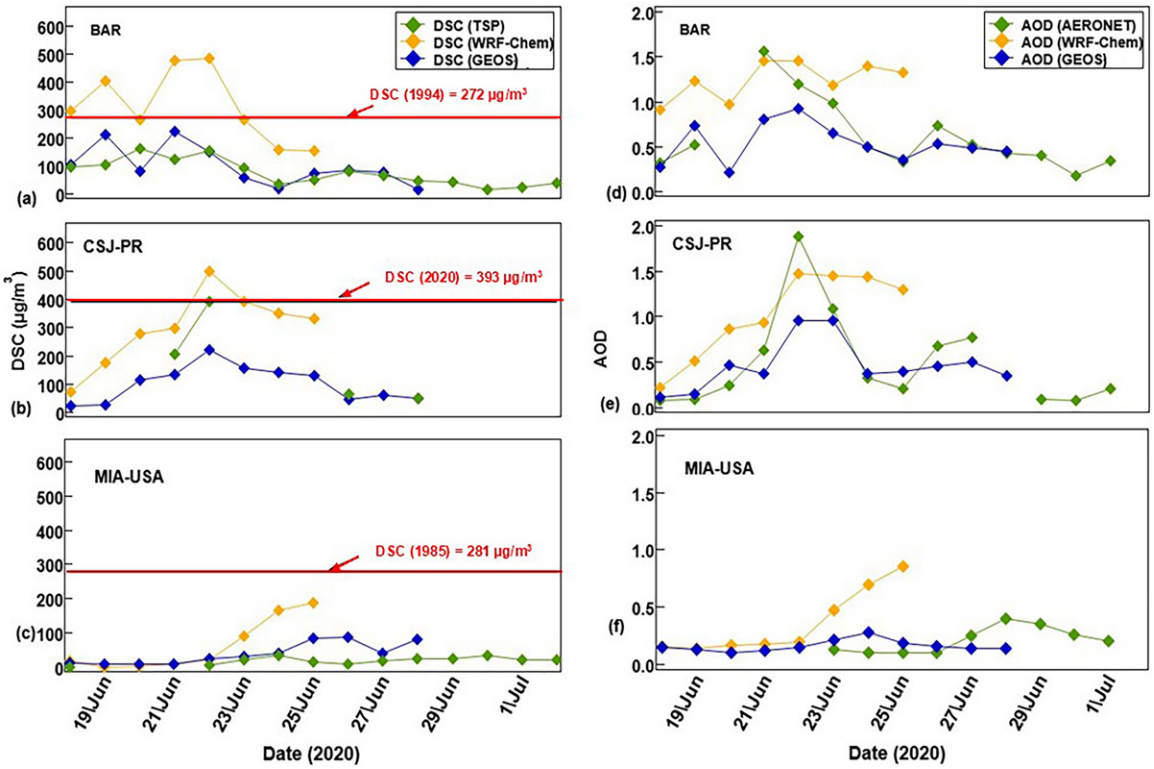

Fig. 17. DSCs measured (TSP; green) and modeled (DSC; WRF-CHEM; yellow; GEOS; blue) at (a) BAR, (b) CSJ–PR, and (c) MIA–USA during 18 Jun–2 Jul. The red horizontal lines represent the highest registered measured DSC at (a) BAR (272 μg m^{-3} in April 1994), (b) CSJ–PR (393 μg m^{-3} in June 2020), and (c) MIA–USA (281 μg m^{-3} in November 1985). BAR and MIA–USA concentrations are based on the historical records (Zuidema et al. 2019). CSJ–PR is based on the U.S.-EPA historical records in PR and the CSJ–PR data. Dust model AOD outputs initiated on 18 Jun by WRF-Chem (yellow) and GEOS (blue) along with AOD from AERONET (green) for (d) BAR, (e) CSJ–PR, and (f) MIA–USA for 18–28 Jun. (a)–(c) DSC and (d)–(f) AOD forecasts are 7 days (3-h resolution) for WRF-CHEM and 10 days (1-h resolution) for GEOS.

close the gap in global aerosol forcing uncertainty. A similar argument could be made for the particular case of African dust transport across the Atlantic and into the Caribbean. Indeed, although there have been numerous studies reporting airborne observations of dust properties (e.g., DeMott et al. 2003; Nowottnick et al. 2011; Jung et al. 2016), most have been incidental to other flight campaign objectives and not since the 2000 Puerto Rico Dust Experiment (PRIDE; Reid et al. 2003) has there been a dedicated airborne campaign in this region and even that lacked detailed ground-based measurements. Fundamental questions about factors controlling of the dust vertical distribution remain more or less where they have been for over 20 years (e.g., Reid et al. 2002; Colarco et al. 2003), and the more recent appreciation of long-range transport of coarse dust particles (e.g., Ryder et al. 2018; Weinzierl et al. 2017) and their potential impacts on radiative forcing and human health (Adebiyi et al. 2023) further bolster the need for a coordinated observation and modeling strategy in this region that takes advantage of new remote sensing, in situ, and modeling tools that were not available during PRIDE. CALIMA is a step toward this integrative approach, but if anything, the need is amplified by its fortuitous observation of the Godzilla extreme dust event.

CALIMA used a regional approach to study the impact of African dust on air quality in the GCB and beyond. It integrated satellite observations with measurements in a network of 12 surface-based sites along with models to characterize the spatial and temporal variability of dust transport (Fig. 18). The combination of the ground-based measurements with the satellite observations allowed a better understanding of the transport of African dust into the region and its impacts on air quality. Satellites alone cannot make these observations. Space-based lidar coverage is sparse, and the better coverage of imagers provides primarily an AOD product, which does not tell where (vertically) the aerosol is.

This point bears emphasis where modeling is considered because the present models that assimilate aerosol observations in near–real time are primarily assimilating AOD-based products. The ground-based observations CALIMA provides are thus crucial to improving aspects of the modeling. They provide a way to connect the column (AOD) to the surface (DSC) that is not possible from the satellites alone. For example, DSC and AOD were predicted using

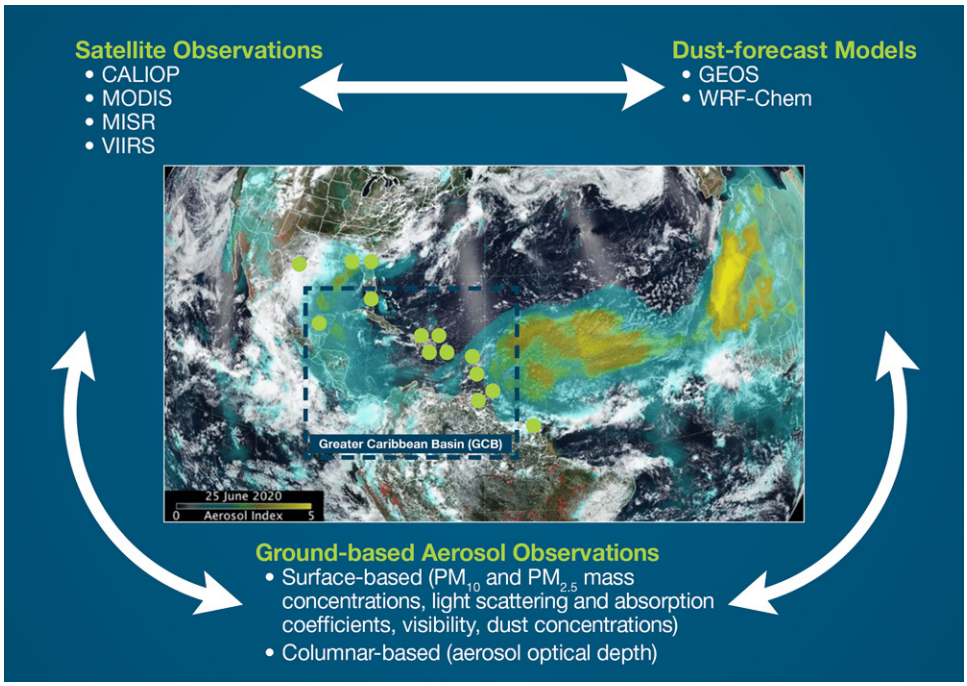

Fig. 18. Progression and extent of the Godzilla dust event, ground-based CALIMA and non-CALIMA stations, ground-based and satellite observations, and dust forecast models. Source for the satellite image: OMPS aerosol index and the VIIRS visible image both from NASA/NOAA's *Suomi NPP* satellite on 25 Jun.

TABLE 3. Maximum AOD and DSC predicted by models (WRF-Chem and GEOS), AERONET AOD, and DSC from TSP filter analyses collected for the stations BAR, CSJ–PR, and MIA–USA during the Godzilla dust event.

	Maximum AOD				Maximum DSC (μg m^{-3})			
Stations	WRF-Chem, date	GEOS, date	AERONET, date	Ratio (WRF-Chem/GEOS)	WRF-Chem, date	GEOS, date	TSP date	Ratio (WRF-Chem/GEOS)
BAR	1.46, 21 Jun	0.92, 22 Jun	1.5, 21 Jun	1.58	484, 22 Jun	149, 22 Jun	161, 20 Jun	3.25
CSJ–PR	1.47, 22 Jun	0.96, 23 Jun	2.0, 22 Jun	1.53	500, 22 Jun	220, 22 Jun	393, 22 Jun	2.27
MIA–USA	0.86, 25 Jun	0.28, 24 Jun	0.4, 28 Jun	3.07	189, 25 Jun	89, 26 Jun	34, 30 Jun	2.12

WRF-Chem and GEOS for BAR, CSJ–PR, and MIA–USA (Table 3, Figs. 17d–f). The DSC predicted by WRF-Chem was about a factor of 2–3 higher than the GEOS DSC at all stations. WRF-Chem and GEOS DSC for BAR and CSJ–PR showed better agreement [correlation coefficients (r): 0.5–0.9] with the dust concentrations than for AOD. Nonetheless, both models showed good correlations (r: 0.6–0.7) with the AOD observed by AERONET (Table ST1). WRF-Chem simulated AOD was 1.5–3 times higher than AOD predicted by GEOS.

The Caribbean Basin provides an ideal site in which to study the long-range transport of African dust and the factors controlling African dust emissions and their long-range impact on health and environmental properties and processes. Excluding a few sites impacted by local sources of dust, the dominant dust in the region is unquestionably from Africa. There is no other distal region that is so frequently and consistently impacted by African dust. Therefore, it is an ideal region in which to monitor emissions from the world's largest dust source and to use these data to further develop that models that will be needed to assess the impact of dust on public health and to be able to issue health alerts.

5. Conclusions

Measurements of African dust during Godzilla and in previous studies raise concerns about the impact of dust on public health and the ability of public health officials to anticipate dust events with sufficient skill to be able to issue alerts with confidence so that susceptible individuals can take precautions. While the GEOS and WRF-Chem models used in CALIMA showed some skills in predicting surface and columnar dust properties during Godzilla, the results revealed large differences between these surface dust forecasts, an issue that needs to be addressed before they can be reliably used for early warnings to protect public health. Although our study is limited to two models, our results are indicative of a general problem in the development of dust models. A recent intercomparison of 16 climate models, for instance, shows that estimated global dust emissions differed by a factor of five (Zhao et al. 2022).

The Godzilla event demonstrates the value of using a regional approach to aerosol studies, one that integrates satellite observations with measurements in a network of surface-based sites along with models to characterize the spatial and temporal variability of dust transport. At present, forecast models that assimilate aerosol data are generally constrained only by measurements of the column aerosol optical depth. There is a need to evaluate and calibrate these models using surface-level observations of dust properties including optical properties which are important to understanding the role of dust in climate forcing. Such studies will also be essential for us to be able to follow changes in dust transport linked to climate variability. Although this paper focuses on the impact of African dust on a specific region, the tracking of African dust activity is important in a larger sense because North Africa is the world's largest dust source, accounting for 28%–69% of global dust emissions (Zhao et al. 2022). Thus, changes in dust transport and properties to the Caribbean Basin can serve as an indicator of African emissions relevant to the global dust loading and its impacts on downwind regions.

Acknowledgments. This work was supported by the NASA ROSES Applied Science, Health, and Air Quality Program Grant 80NSSC19K0194 and the U.S. Department of Energy (DOE), Office of Science, Office of Biological and Environmental Research (OBER), and Atmospheric System Research Program under Contract DE-SC0012704. The CALIMA project acknowledges the support of the NOAA National Weather Service—San Juan Office for the daily weather forecasts. E. A. was supported by the NOAA cooperative agreement with the Cooperative Institute for Research in Environmental Sciences (CIRES; Grant NA22OAR4320151). P. R. C. is supported by the NASA Chemistry Climate Modeling work package supported by the Modeling and Analysis Program (PM: D. Considine) and by a NASA Weather Research and Atmospheric Dynamics grant (PI: E. Nowottnick). H. Y. was supported by the NASA CALIPSO/CloudSat Science Team program. L. D.'s support under Subcontract 1474871 with the Jet Propulsion Laboratory, the California Institute of Technology, is gratefully acknowledged. The group from the UNAM acknowledges the support of the Consejo Nacional de Ciencia y Tecnología and the Dirección General de Asuntos del Personal Académico through Grants FC-2164 and PAPIIT IN111120, respectively. We also thank the University Network of Atmospheric Observatories (RUOA) for the MEDA ground-based data. L. A. L. acknowledges support from Maximizing Access to Research Careers (MARC) Grant 5T34GM007821-40S1 and NSF CAREER Grant AGS-1944958. P. Z. acknowledges support from NOAA OAR CPO Grant NA19OAR4310379. This research was supported by the Atmospheric Radiation Measurement (ARM) user facility, a U.S. Department of Energy (DOE) Office of Science user facility managed by the Biological and Environmental Research program. Specifically, we thank ARM for the loan of the SeaTainer through the project.

Data availability statement. The Puerto Rico ground-based aerosol data (particle concentrations, scattering, and absorption) are available on the EBAS webpage (https://ebas-data.nilu.no/; last access: 10 March 2024). PM_{10} and $PM_{2.5}$ data from CAY, TRI, TOB, MAR, GUA, MEDA–MEX, HOU–USA, FLO-NE, CSJ–PR, CAT–PR, GUAY + MAYA–PR are available on request to the corresponding author and also available from https://www.epa.gov/outdoor-air-quality-data/air-data-concentration-plot and https://www.iqair.com/air-quality-map?lat=18.46633&lng=-66.10572&zoomLevel=10. The Miami/Barbados lidar data are available upon request from P. Z. and I. S., respectively. AERONET data from Barbados, Guadeloupe, Puerto Rico, Tallahassee–Florida, and Miami are available from the AERONET website. The CALIOP aerosol products were obtained from the NASA Langley Research Center Atmospheric Science Data Center (https://doi.org/10.5067/CALIOP/CALIPSO/CAL_LID_L2_05kmAPro-Standard-V4-21, NASA/LARC/SD/ASDC, 2018). The MODIS level 2 aerosol products are archived by NASA and freely available to the public at https://www.earthdata.nasa.gov/. MISR level 3 aerosol products are archived by NASA and freely available to the public at https://www.earthdata.nasa.gov/. MISR level 3 aerosol products are archived by NASA and freely available to the public at https://www.earthdata.nasa.gov/. GEOS forecast data were downloaded from https://fluid.nccs.nasa.gov/missions/custom_mission%2BPRDUST/?fcst=20240327T060000&tau=000&streamG5FPFC&level=0&field=fineaot&region=prdust_i. CIMH WRF-Chem model inquiries and requests at https://dafc.cimh.edu.bb/contact/. Any other CALIMA are available from the corresponding author upon reasonable request (omayol@bnl.gov).

References

Adebiyi, A., and Coauthors, 2023: A review of coarse mineral dust in the Earth system. *Aeolian Res.*, **60**, 100849, https://doi.org/10.1016/j.aeolia.2022.100849.

Akpinar-Elci, M., F. E. Martin, J. G. Behr, and R. Diaz, 2015: Saharan dust, climate variability, and asthma in Grenada, the Caribbean. *Int. J. Biometeor.*, **59**, 1667–1671, https://doi.org/10.1007/s00484-015-0973-2.

Alicea-Alvarez, N., B. Swanson-Biearman, and S. G. Kelsen, 2014: A review of barriers to effective asthma management in Puerto Ricans: Cultural, healthcare system and pharmacogenomic issues. *J. Asthma*, **51**, 97–105, https://doi.org/10.3109/02770903.2013.845205.

Andrews, E., and Coauthors, 2019: Overview of the NOAA/ESRL Federated Aerosol Network. *Bull. Amer. Meteor. Soc.*, **100**, 123–135, https://doi.org/10.1175/BAMS-D-17-0175.1.

Banks, J. R., A. Hünerbein, B. Heinold, H. E. Brindley, H. Deneke, and K. Schepanski, 2019: The sensitivity of the colour of dust in MSG-SEVIRI desert dust infrared composite imagery to surface and atmospheric conditions. *Atmos. Chem. Phys.*, **19**, 6893–6911, https://doi.org/10.5194/acp-19-6893-2019.

Barreto, Á., and Coauthors, 2022: Long-term characterisation of the vertical structure of the Saharan Air Layer over the Canary Islands using lidar and radiosonde profiles: Implications for radiative and cloud processes over the subtropical Atlantic Ocean. *Atmos. Chem. Phys.*, **22**, 739–763, https://doi.org/10.5194/acp-22-739-2022.

Bozlaker, A., J. M. Prospero, M. P. Fraser, and S. Chellam, 2013: Quantifying the contribution of long-range Saharan dust transport on particulate matter concentrations in Houston, Texas, using detailed elemental analysis. *Environ. Sci. Technol.*, **47**, 10179–10187, https://doi.org/10.1021/es4015663.

Cadelis, G., R. Tourres, and J. Molinie, 2014: Short-term effects of the particulate pollutants contained in Saharan dust on the visits of children to the emergency department due to asthmatic conditions in Guadeloupe (French archipelago of the Caribbean). *PLOS ONE*, **9**, e91136, https://doi.org/10.1371/journal.pone.0091136.

Camino, C., and Coauthors, 2015: An empirical equation to estimate mineral dust concentrations from visibility observations in Northern Africa. *Aeolian Res.*, **16**, 55–68, https://doi.org/10.1016/j.aeolia.2014.11.002.

Carlson, T. N., and J. M. Prospero, 1972: The large-scale movement of Saharan air outbreaks over the northern equatorial Atlantic. *J. Appl. Meteor.*, **11**, 283–297, https://doi.org/10.1175/1520-0450(1972)011<0283:TLSMOS>2.0.CO;2.

Castellanos, P., and Coauthors, 2024: Mineral dust optical properties for remote sensing and global modeling: A review. *Remote Sens. Environ.*, **303**, 113982, https://doi.org/10.1016/j.rse.2023.113982.

Chauvin, F., R. Roehrig, and J.-P. Lafore, 2010: Intraseasonal variability of the Saharan heat low and its link with midlatitudes. *J. Climate*, **23**, 2544–2561, https://doi.org/10.1175/2010JCLI3093.1.

Chen, T.-C. T., 2005: Maintenance of the midtropospheric North African summer circulation: Saharan high and African easterly jet. *J. Climate*, **18**, 2943–2962, https://doi.org/10.1175/JCLI3446.1.

Colarco, P., and Coauthors, 2003: Saharan dust transport to the Caribbean during PRIDE: 2. Transport, vertical profiles, and deposition in simulations of in situ and remote sensing observations. *J. Geophys. Res.*, **108**, 8590, https://doi.org/10.1029/2002JD002659.

Crews, S. C., and L. A. Esposito, 2020: Towards a synthesis of the Caribbean biogeography of terrestrial arthropods. *BMC Evol. Biol.*, **20**, 12, https://doi.org/10.1186/s12862-019-1576-z.

Cuevas, E., A. J. Gómez-Peláez, S. Rodríguez, E. Terradellas, S. Basart, R. D. García, O. E. García, and S. Alonso-Pérez, 2017: The pulsating nature of large-scale Saharan dust transport as a result of interplays between mid-latitude Rossby waves and the North African dipole intensity. *Atmos. Environ.*, **167**, 586–602, https://doi.org/10.1016/j.atmosenv.2017.08.059.

Delgadillo, R., K. J. Voss, and P. Zuidema, 2018: Characteristics of optically thin coastal Florida cumuli derived from surface-based lidar measurements. *J. Geophys. Res. Atmos.*, **123**, 10591–10605, https://doi.org/10.1029/2018JD028867.

DeMott, P., K. Sassen, M. Poellot, D. Baumgardner, D. Rogers, S. Brooks, A. Prenni, and S. Kreidenweis, 2003: African dust aerosols as atmospheric ice nuclei. *Geophys. Res. Lett.*, **30**, 1732, https://doi.org/10.1029/2003GL017410.

Denjean, C., and Coauthors, 2016: Size distribution and optical properties of African mineral dust after intercontinental transport. *J. Geophys. Res. Atmos.*, **121**, 7117–7138, https://doi.org/10.1002/2016JD024783.

Dey, S., and L. Di Girolamo, 2010: A climatology of aerosol optical and microphysical properties over the Indian subcontinent from 9 years (2000-2008) of Multiangle Imaging SpectroRadiometer (MISR) data. *J. Geophys. Res.*, **115**, D15204, https://doi.org/10.1029/2009JD013395.

Dunion, J. P., and C. S. Velden, 2004: The impact of the Saharan air layer on Atlantic tropical cyclone activity. *Bull. Amer. Meteor. Soc.*, **85**, 353–366, https://doi.org/10.1175/BAMS-85-3-353.

Evan, A. T., G. R. Foltz, D. Zhang, and D. J. Vimont, 2011: Influence of African dust on ocean–atmosphere variability in the tropical Atlantic. *Nat. Geosci.*, **4**, 762–765, https://doi.org/10.1038/ngeo1276.

——, C. Flamant, S. Fiedler, and O. Doherty, 2014: An analysis of aeolian dust in climate models. *Geophys. Res. Lett.*, **41**, 5996–6001, https://doi.org/10.1002/2014GL060545.

Francis, D., R. Fonseca, N. Nelli, J. Cuesta, M. Weston, A. Evan, and M. Temimi, 2020: The atmospheric drivers of the major Saharan dust storm in June 2020. *Geophys. Res. Lett.*, **47**, e2020GL090102, https://doi.org/10.1029/2020GL090102.

Garay, M. J., and Coauthors, 2020: Introducing the 4.4 km spatial resolution Multi-Angle Imaging SpectroRadiometer (MISR) aerosol product. *Atmos. Meas. Tech.*, **13**, 593–628, https://doi.org/10.5194/amt-13-593-2020.

Gaztambide-Géigel, A., 2004: The invention of the Caribbean in the 20th century (the definitions of the Caribbean as a historical and methodological problem). *Soc. Econ. Stud.*, **53**, 127–157.

Gutleben, M., and S. Gross, 2021: Turbulence analysis in long-range-transported Saharan dust layers with airborne lidar. *Geophys. Res. Lett.*, **48**, e2021GL094418, https://doi.org/10.1029/2021GL094418.

Holben, B. N., and Coauthors, 1998: AERONET—A federated instrument network and data archive for aerosol characterization. *Remote Sens. Environ.*, **66** (1), 1–16, https://doi.org/10.1016/S0034-4257(98)00031-5.

Huang, J., C. Zhang, and J. M. Prospero, 2010: African dust outbreaks: A satellite perspective of temporal and spatial variability over the tropical Atlantic Ocean. *J. Geophys. Res.*, **115**, D05202, https://doi.org/10.1029/2009JD012516.

Jung, E., B. A. Albrecht, G. Feingold, H. H. Jonsson, P. Chuang, and S. L. Donaher, 2016: Aerosols, clouds, and precipitation in the North Atlantic trades observed during the Barbados aerosol cloud experiment—Part 1: Distributions and variability. *Atmos. Chem. Phys.*, **16**, 8643–8666, https://doi.org/10.5194/acp-16-8643-2016.

Kahn, R. A., and Coauthors, 2009: MISR aerosol product attributes and statistical comparisons with MODIS. *IEEE Trans. Geosci. Remote Sens.*, **47**, 4095–4114, https://doi.org/10.1109/TGRS.2009.2023115.

——, and Coauthors, 2023: Reducing aerosol forcing uncertainty by combining models with satellite and within-the-atmosphere observations: A three-way street. *Rev. Geophys.*, **61**, https://doi.org/10.1029/2022RG000796.

Kim, D., and Coauthors, 2014: Sources, sinks, and transatlantic transport of North African dust aerosol: A multimodel analysis and comparison with remote sensing data. *J. Geophys. Res. Atmos.*, **119**, 6259–6277, https://doi.org/10.1002/2013JD021099.

Kok, J. F., T. Storelvmo, V. A. Karydis, A. A. Adebiyi, N. M. Mahowald, A. T. Evan, C. He, and D. M. Leung, 2023: Mineral dust aerosol impacts on global climate and climate change. *Nat. Rev. Earth Environ.*, **4**, 71–86, https://doi.org/10.1038/s43017-022-00379-5.

Kramer, S. J., and Coauthors, 2020a: Apparent dust size discrepancy in aerosol reanalysis in North African dust after long-range transport. *Atmos. Chem. Phys.*, **20**, 10 047–10 062, https://doi.org/10.5194/acp-20-10047-2020.

——, B. P. Kirtman, P. Zuidema, and F. Ngan, 2020b: Subseasonal variability of elevated dust concentrations over South Florida. *J. Geophys. Res. Atmos.*, **125**, 10 047–10 062, https://doi.org/10.1029/2019JD031874.

Levy, R. C., L. A. Munchak, S. Mattoo, F. Patadia, L. A. Remer, and R. E. Holz, 2015: Towards a long-term global aerosol optical depth record: Applying a consistent aerosol retrieval algorithm to MODIS and VIIRS-observed reflectance. *Atmos. Meas. Tech.*, **8**, 4083–4110, https://doi.org/10.5194/amt-8-4083-2015.

Lwin, K. S., and Coauthors, 2023: Effects of desert dust and sandstorms on human health: A scoping review. *Geohealth*, **7**, e2022GH000728, https://doi.org/10.1029/2022GH000728.

Mehra, M., and Coauthors, 2023: Atmospheric heating in the US from Saharan dust: Tracking the June 2020 event with surface and satellite observations. *Atmos. Environ.*, **310**, 119988, https://doi.org/10.1016/j.atmosenv.2023.119988.

Met Office: EUMETSAT, 2022: MSG: Dust imagery in the RGB channels over the full disc at 41.5 degrees East (LEDF41, up to 0900UTC 1st June 2022). NERC EDS Centre for Environmental Data Analysis, accessed 30 August 2024, https://catalogue.ceda.ac.uk/uuid/b1dacc09b42f4d8ab492c5d5c751efa9.

Molod, A., L. Takacs, M. Suarez, and J. Bacmeister, 2015: Development of the GEOS-5 atmospheric general circulation model: Evolution from MERRA to MERRA2. *Geosci. Model Dev.*, **8**, 1339–1356, https://doi.org/10.5194/gmd-8-1339-2015.

Monteil, M. A., G. Joseph, C. Changkit, G. Wheeler, and R. M. Antoine, 2005: Comparison of prevalence and severity of asthma among adolescents in the Caribbean islands of Trinidad and Tobago: Results of a nationwide cross-sectional survey. *BMC Public Health*, **5**, 96, https://doi.org/10.1186/1471-2458-5-96.

Nkemdirim, L. C., 1997: Climate and life in the Caribbean basin. *Climates and Societies—A Climatological Perspective*, M. Yoshino et al., Eds., The GeoJournal Library, Vol. 36, Springer, https://doi.org/10.1007/978-94-017-1055-8_9.

Nowottnick, E., P. Colarco, A. da Silva, D. Hlavka, and M. McGill, 2011: The fate of Saharan dust across the Atlantic and implications for a central American dust barrier. *Atmos. Chem. Phys.*, **11**, 8415–8431, https://doi.org/10.5194/acp-11-8415-2011.

Okin, G. S., and Coauthors, 2011: Impacts of atmospheric nutrient deposition on marine productivity: Roles of nitrogen, phosphorus, and iron. *Global Biogeochem. Cycles*, **25**, GB2022, https://doi.org/10.1029/2010GB003858.

Prospero, J. M., 1999: Long-term measurements of the transport of African mineral dust to the southeastern United States: Implications for regional air quality. *J. Geophys. Res.*, **104**, 15 917–15 927, https://doi.org/10.1029/1999JD900072.

——, and T. N. Carlson, 1972: Vertical and areal distribution of Saharan dust over the western equatorial North Atlantic Ocean. *J. Geophys. Res.*, **77**, 5255–5265, https://doi.org/10.1029/JC077i027p05255.

——, and P. J. Lamb, 2003: African droughts and dust transport to the Caribbean: Climate change implications. *Science*, **302**, 1024–1027, https://doi.org/10.1126/science.1089915.

——, and O. L. Mayol-Bracero, 2013: Understanding the transport and impact of African dust on the Caribbean basin. *Bull. Amer. Meteor. Soc.*, **94**, 1329–1337, https://doi.org/10.1175/BAMS-D-12-00142.1.

——, R. Glaccum, and R. Nees, 1981: Atmospheric transport of soil dust from Africa to South America. *Nature*, **289**, 570–572, https://doi.org/10.1038/289570a0.

——, R. T. Nees, and M. Uematsu, 1987: Deposition rate of particulate and dissolved aluminum derived from Saharan dust in precipitation at Miami, Florida. *J. Geophys. Res.*, **92**, 14 723–14 731, https://doi.org/10.1029/JD092iD12p14723.

——, I. Olmez, and M. Ames, 2001: Al and Fe in $PM_{2.5}$ and PM_{10} suspended particles in south-central Florida: The impact of the long range transport of African mineral dust. *Water Air Soil Pollut.*, **125**, 291–317, https://doi.org/10.1023/A:1005277214288.

——, E. Blades, R. Naidu, G. Mathison, H. Thani, and M. C. Lavoie, 2008: Relationship between African Dust carried in the Atlantic trade winds and surges in pediatric asthma attendances in the Caribbean. *Int. J. Biometeor.*, **52**, 823–832, https://doi.org/10.1007/s00484-008-0176-1.

——, F. X. Collard, J. Molinié, and A. Jeannot, 2014: Characterizing the annual cycle of African dust transport to the Caribbean basin and South America and its impact on the environment and air quality. *Global Biogeochem. Cycles*, **28**, 757–773, https://doi.org/10.1002/2013GB004802.

——, A. C. Delany, A. C. Delany, and T. N. Carlson, 2021: The discovery of African dust transport to the Western Hemisphere and the Saharan air layer: A history. *Bull. Amer. Meteor. Soc.*, **102**, E1239–E1260, https://doi.org/10.1175/BAMS-D-19-0309.1.

Pu, B., and Q. Jin, 2021: A record-breaking trans-Atlantic African dust plume associated with atmospheric circulation extremes in June 2020. *Bull. Amer. Meteor. Soc.*, **102**, E1340–E1356, https://doi.org/10.1175/BAMS-D-21-0014.1.

Raga, G. B., and Coauthors, 2021: ADABBOY: African dust and biomass burning over Yucatan. *Bull. Amer. Meteor. Soc.*, **102**, E1543–E1556, https://doi.org/10.1175/BAMS-D-20-0172.1.

Reid, J., and Coauthors, 2002: Dust vertical distribution in the Caribbean during the Puerto Rico Dust Experiment. *Geophys. Res. Lett.*, **29**, 1151, https://doi.org/10.1029/2001GL014092.

——, and Coauthors, 2003: Analysis of measurements of Saharan dust by airborne and ground-based remote sensing methods during the Puerto Rico Dust Experiment (PRIDE). *J. Geophys. Res.*, **108**, 8586, https://doi.org/10.1029/2002JD002493.

Robertson, D. R., and K. L. Cramer, 2014: Defining and dividing the Greater Caribbean: Insights from the biogeography of shorefishes. *PLOS ONE*, **9**, e102918, https://doi.org/10.1371/journal.pone.0102918.

Rodríguez, S., E. Cuevas, J. M. Prospero, A. Alastuey, X. Querol, J. López-Solano, M. I. García, and S. Alonso-Pérez, 2015: Modulation of Saharan dust export by the North African dipole. *Atmos. Chem. Phys.*, **15**, 7471–7486, https://doi.org/10.5194/acp-15-7471-2015.

Ryder, C. L., 2021: Radiative effects of increased water vapor in the upper Saharan air layer associated with enhanced dustiness. *J. Geophys. Res. Atmos.*, **126**, e2021JD034696, https://doi.org/10.1029/2021JD034696.

——, and Coauthors, 2018: Coarse-mode mineral dust size distributions, composition and optical properties from AER-D aircraft measurements over the tropical eastern Atlantic. *Atmos. Chem. Phys.*, **18**, 17 225–17 257, https://doi.org/10.5194/acp-18-17225-2018.

Schepanski, K., I. Tegen, B. Laurent, B. Heinold, and A. Macke, 2007: A new Saharan dust source activation frequency map derived from MSG-SEVIRI IR-channels. *Geophys. Res. Lett.*, **34**, L18803, https://doi.org/10.1029/2007GL030168.

——, ——, M. C. Todd, B. Heinold, G. Bönisch, B. Laurent, and A. Macke, 2009: Meteorological processes forcing Saharan dust emission inferred from MSG-SEVIRI observations of subdaily dust source activation and numerical models. *J. Geophys. Res.*, **114**, D10201, https://doi.org/10.1029/2008JD010325.

——, B. Heinold, and I. Tegen, 2017: Harmattan, Saharan heat low, and West African monsoon circulation: Modulations on the Saharan dust outflow towards the North Atlantic, Atmos. *Chem. Phys.*, **17**, 10 223–10 243, https://doi.org/10.5194/acp-17-10223-2017.

Skamarock, W. C., J. B. Klemp, J. Dudhia, D. O. Gill, D. M. Barker, W. Wang, and J. G. Powers, 2005: A description of the Advanced Research WRF version 2. NCAR Tech. Note NCAR/TN-468+STR, 88 pp., https://doi.org/10.5065/D6DZ069T.

Stein, A. F., R. R. Draxler, G. D. Rolph, B. J. B. Stunder, M. D. Cohen, and F. Ngan, 2015: NOAA's HYSPLIT atmospheric transport and dispersion modeling system. *Bull. Amer. Meteor. Soc.*, **96**, 2059–2077, https://doi.org/10.1175/BAMS-D-14-00110.1.

Stevens, B., and Coauthors, 2016: The Barbados Cloud Observatory: Anchoring investigations of clouds and circulation on the edge of the ITCZ. *Bull. Amer. Meteor. Soc.*, **97**, 787–801, https://doi.org/10.1175/BAMS-D-14-00247.1.

Tong, D. Q., and Coauthors, 2023: Health and safety effects of airborne soil dust in the Americas and beyond. *Rev. Geophys.*, **61**, e2021RG000763, https://doi.org/10.1029/2021RG000763.

Twohy, C. H., and Coauthors, 2009: Saharan dust particles nucleate droplets in eastern Atlantic clouds. *Geophys. Res. Lett.*, **36**, L01807, https://doi.org/10.1029/2008GL035846.

Ward, N., A. H. Fink, R. J. Keane, and D. J. Parker, 2023: Upper-level midlatitude troughs in boreal winter have an amplified low-latitude linkage over Africa. *Atmos. Sci. Lett.*, **24**, e1129, https://doi.org/10.1002/asl.1129.

Weinzierl, B., and Coauthors, 2017: The Saharan aerosol long-range transport and aerosol–cloud-interaction experiment: Overview and selected highlights. *Bull. Amer. Meteor. Soc.*, **98**, 1427–1451, https://doi.org/10.1175/BAMS-D-15-00142.1.

West, J. J., and Coauthors, 2016: What we breathe impacts our health: Improving understanding of the link between air pollution and health. *Environ. Sci. Technol.*, **50**, 4895–4904, https://doi.org/10.1021/acs.est.5b03827.

WHO, 2021: WHO global air quality guidelines: Particulate matter ($PM_{2.5}$ and PM_{10}), ozone, nitrogen dioxide, sulfur dioxide and carbon monoxide – Executive summary. World Health Organization, 28 pp., https://www.who.int/publications/i/item/9789240034228.

Winker, D. M., M. A. Vaughan, A. Omar, Y. Hu, K. A. Powell, Z. Liu, W. H. Hunt, and S. A. Young, 2009: Overview of the CALIPSO mission and CALIOP data processing algorithms. *J. Atmos. Oceanic Technol.*, **26**, 2310–2323, https://doi.org/10.1175/2009JTECHA1281.1.

Xian, P., and Coauthors, 2019: Current state of the global operational aerosol multi-model ensemble: An update from the International Cooperative for Aerosol Prediction (ICAP). *Quart. J. Roy. Meteor. Soc.*, **145**, 176–209, https://doi.org/10.1002/qj.3497.

Yu, H., and Coauthors, 2015a: Quantification of trans-Atlantic dust transport from seven-year (2007–2013) record of CALIPSO lidar measurements. *Remote Sens. Environ.*, **159**, 232–249, https://doi.org/10.1016/j.rse.2014.12.010.

——, and Coauthors, 2015b: The fertilizing role of African dust in the Amazon rainforest: A first multiyear assessment based on data from cloud-aerosol lidar and infrared pathfinder satellite observations. *Geophys. Res. Lett.*, **42**, 1984–1991, https://doi.org/10.1002/2015GL063040.

——, and Coauthors, 2019: Estimates of African dust deposition along the trans-Atlantic transit using the decade-long record of aerosol measurements from CALIOP, MODIS, MISR, and IASI. *J. Geophys. Res. Atmos.*, **124**, 7975–7996, https://doi.org/10.1029/2019JD030574.

——, and Coauthors, 2021: Observation and modeling of the historic "Godzilla" African dust intrusion into the Caribbean Basin and the southern US in June 2020. *Atmos. Chem. Phys.*, **21**, 12 359–12 383, https://doi.org/10.5194/acp-21-12359-2021.

Zhang, X., L. Zhao, D. Q. Tong, G. Wu, M. Dan, and B. Teng, 2016: A systematic review of global desert dust and associated human health effects. *Atmosphere*, **7**, 158, https://doi.org/10.3390/atmos7120158.

Zhao, A., C. L. Ryder, and L. J. Wilcox, 2022: How well do the CMIP6 models simulate dust aerosols? *Atmos. Chem. Phys.*, **22**, 2095–2119, https://doi.org/10.5194/acp-22-2095-2022.

Zuidema, P., C. Alvarez, S. J. Kramer, L. Custals, M. Izaguirre, P. Sealy, J. M. Prospero, and E. Blades, 2019: Is summer African dust arriving earlier to Barbados? The updated long-term in situ dust mass concentration time series from ragged point, Barbados, and Miami, Florida. *Bull. Amer. Meteor. Soc.*, **100**, 1981–1986, https://doi.org/10.1175/BAMS-D-18-0083.1.